Equilibria for a two-dimensional aggregation model with two species

Joep H.M. Evers Razvan C. Fetecau Theodore Kolokolnikov

August 1, 2017

Abstract

We consider an aggregation model for two interacting species. The coupling between the species is via their velocities, that incorporate self- and cross-interactions. Our main interest is categorizing the possible steady states of the considered model in two dimensions. Notably, we identify their regions of existence and stability in the parameter space. For assessing the stability we use a combination of variational tools (based on the gradient flow formulation of the model and the associated energy), and linear stability analysis (perturbing the boundaries of the species' supports). We rely on numerical investigations for those steady states that are not analytically tractable. Finally we perform a two-scale expansion to characterize the steady state in the limit of asymptotically weak cross-interactions.

Keywords: multi-species models, swarm equilibria, energy minimizers, gradient flow, linear stability, asymptotic analysis

1 Introduction

In this paper we consider a two-species aggregation model in the form of a system of partial differential equations[1]:

$$\frac{\partial \rho_1}{\partial t} + \nabla \cdot (\rho_1 v_1) = 0, \quad v_1 = -\nabla K_s * \rho_1 - \nabla K_c * \rho_2, \tag{1a}$$

$$\frac{\partial \rho_2}{\partial t} + \nabla \cdot (\rho_2 v_2) = 0, \quad v_2 = -\nabla K_c * \rho_1 - \nabla K_s * \rho_2. \tag{1b}$$

Here, ρ_1 and ρ_2 are the densities of the two species, K_s and K_c are self- and cross-interaction potentials, and the asterisk $*$ denotes convolution. The self-interaction potential K_s models inter-individual social interactions within the same species, while K_c models interactions between individuals of different species. Typically, interaction potentials are assumed to be symmetric, and also, to model long-range attraction and short-range repulsion. Model (1) applies to arbitrary spatial dimension.

Our main motivation for studying this model is the self-organization occurring in aggregates of biological cells. Experimentally observed sorting of embryonic cells has been documented in various works [1, 29]; we also refer to Figure 1 in [11] for a schematic overview of possible patterns of two species of certain embryonic cells. These patterns range from complete mixing at the cell level, to full separation of the two species. The major goal of the present paper is to investigate equilibrium solutions, along with their stability, using model (1) in two spatial dimensions. The nonlocality in our model resembles that in e.g. [1, 38].

[1]Strictly speaking, these equations are integro-differential equations due to the nonlocality (convolutions) in the expressions for v_1 and v_2. Throughout this paper we will refer to (1) as a 'PDE model', though.

The one-species analogue of (1) is a mathematical model for collective behaviour that has seen a surge of attention in recent literature. A variety of issues have been studied for the one-species model, such as the well-posedness of solutions [9, 8, 13, 23], equilibria and long-time behaviour [36, 26, 40, 25], blow-up (in finite or infinite time) by mass concentration [24, 6, 30], existence and characterization of global minimizers for the associated interaction energy [2, 16, 12, 39], and passage from discrete to continuum by mean-field limits [14]. A particularly appealing aspect of the model is that despite its simplicity, its solutions can exhibit complex behaviour and can capture a wide variety of "swarm" behaviour. Provoking and motivational galleries of solutions that can be obtained with the one species model can be found for instance in [34, 40]. They include aggregations on disks, annuli, rings, soccer balls, and many others.

Despite the intensive activity on the one-species model, its extensions to multiple species have remained largely unexplored. From an analysis viewpoint, the well-posedness of solutions to multi-species aggregation models of type (1) has been recently considered in various works [21, 19]. The general setup is to investigate existence and uniqueness of weak measure solutions using tools from optimal mass transportation such as Wasserstein distance(s). In particular, the authors of [21] consider a more general model where the two species have distinct self-interaction potentials, and cross-interaction potentials that are a scalar multiple of each other. They show, under certain assumptions on the potentials, that the two-species aggregation model represents a gradient flow with respect to a modified Wasserstein distance of an interaction energy that comprises self- and cross-interaction terms.

Two-species models similar to (1) have been studied recently in the context of predator-prey dynamics [15, 22]. To model such interactions one needs to consider cross-interaction potentials that have opposite signs, so that the predator is attracted to prey, while the prey is repelled by it. Both [15] and [22] show very intricate patterns that form dynamically (and at equilibrium) with such predator-prey systems. Note that in model (1), the cross-interaction potential K_c is not restricted to be exclusively attractive or repulsive; the particular form considered in the sequel includes in fact both attractive and repulsive cross-interactions between the two species.

The present study focuses on the aggregation model (1) in two dimensions, with self- and cross-interaction potentials K_s and K_c that consist of Newtonian repulsion and quadratic attraction. Specifically, we consider interaction potentials of the form:

$$K_s(x) = -a_s \ln|x| + \frac{b_s}{2}|x|^2, \tag{2a}$$

$$K_c(x) = -a_c \ln|x| + \frac{b_c}{2}|x|^2, \tag{2b}$$

where a_s, b_s represent the magnitudes of self-attraction and self-repulsion interactions, and similarly, a_c, b_c represent the strengths of cross-attraction and cross-repulsion, respectively. All these parameters are taken to be strictly positive.

Interaction potentials in the form (2) have been studied in various works on the one-species model [24, 26, 25, 31]. It has been demonstrated in [7, 26] that solutions to the one-species aggregation equation, with an interaction potential of form (2a), approach asymptotically a radially symmetric equilibrium that consists in a ball of constant density. More generally, equilibria for interaction potentials in power-law form have been illustrated and investigated in numerous studies on the one-species aggregation model [34, 40, 25, 3].

For the two-species model studied in this paper, potentials in the form (2) also have the remarkable property that they lead to equilibria of constant densities within their supports. Nevertheless, for two species, there is a much more diverse set of such equilibrium configurations, which include both symmetric and non-symmetric states. To offer an early motivation for our study, we introduce briefly Figure 1, which shows a gallery of equilibria that can be obtained with model (1) in two dimensions, for interaction potentials in the form (2).

Figure 1 shows the two populations ρ_1 and ρ_2 in blue circles and red diamonds, respectively. These equilibria were found numerically by using the particle system associated to the PDE

model (1); see Section 2.4 for more details. In the figure, and throughout the paper, we employ the notations:

$$A = \frac{a_c}{a_s}, \quad B = \frac{b_c}{b_s}, \quad M = \frac{M_1}{M_2}, \tag{3}$$

where M_1 and M_2 denote the total masses of the two densities ρ_1 and ρ_2, respectively. Note that M_1 and M_2 do not depend on time, and consequently, are set by the initial densities. This fact can be inferred, at least formally, by integrating over the entire space the two evolution equations in (1a) and (1b) (see also equation (5)). Throughout the paper we take $M_1 > M_2$ (or, by the notation in (3), $M > 1$), so in all illustrations, the heavier species ρ_1 is shown in blue circles, while the lighter species ρ_2 appears in red diamonds.

In Figure 1, the obtained steady states are shown in the (A, B)-phase plane according to their parameter values. The solid and dashed lines and curves in the diagram are relevant for the existence and stability of such steady states (their exact descriptions can be found in Figure 2). The major focus of the present paper is the investigation of several of the equilibria illustrated in Figure 1. Before we present an overview of the results reported herein (see below), let us discuss briefly the two main approaches that we use in our investigations, each with its own merits and limitations.

One approach is to consider the variational interpretation [21], and investigate equilibrium solutions to (1) as stationary points of the interaction energy. To establish whether such stationary points are energy minimizers we adopt and extend the framework developed in [5] for the one-species analogue of model (1). In such setup, the problem reduces to investigating the first and second variations of the energy for various perturbations that may occur. Variational approaches to the one-species aggregation model have received a great deal of interest lately [2, 12, 16, 12, 39], and a few very recent works have also dealt with two-species models [17, 4]. The other approach considered in this work is quite different in spirit, and it consists in a linear stability analysis of the boundaries that enclose the two aggregations. Here, we take advantage of the choice of potentials considered in this paper, consisting of Newtonian repulsion and quadratic attraction, for which the equilibria are made of compactly supported aggregations of constant densities [26]. This approach reduces the dimensionality of the problem, since we focus on the stability of the boundaries of the supports only, for which we find self-contained evolution equations.

The approach to linear stability that we consider in this paper relates to techniques used to study neural field models [27, 28, 18, 10, 20]. In particular in [27] the authors study certain "breather" patterns by looking at the evolution of their boundaries. They also use azimuthal perturbations to analyze their stability – see Section 2.3 for more details and further discussion of this literature. Our approach also relates to previous works of one of the authors of the current paper. Specifically, in [15], a technique similar to the one used in the current paper is used to perturb the boundaries of a compactly supported swarm density. In [37] the authors study the stability of equilibria supported on one-dimensional curves for the class of aggregation models considered in his paper. In both [34] and [33], the authors perturb a finite number of discrete points on a circle. Their algebraic descriptions can however be generalized to a (continuous) circular curve, and the formulas can moreover be rewritten exactly in the form we use (including the Fourier decomposition; cf. (28) and (35)). We apply this procedure to a particular equilibrium that resembles the image of a target used for shooting or archery (see e.g. Figure 4); henceforth, we simply call such configuration a "target".

Overview of the results of the paper. The results of this paper concern steady states of model (1) –in two dimensions, with interaction potentials (2)– and their stability as the interaction parameters are varied. The phase plane in Figure 2 is subdivided into the relevant parameter regimes D_1 to D_6. These regions are bounded by the solid lines in the figure whose equations are given in terms of A, B and M introduced in (3).

We note that in the variational approach, for most of the parameter space we had to restrict

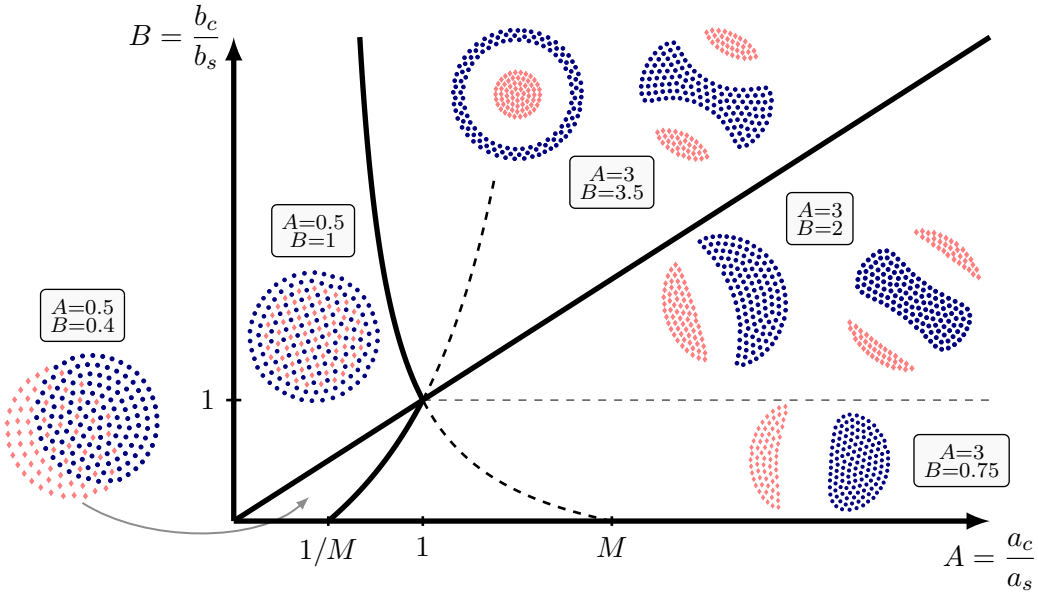

Figure 1: Overview of steady states of model (1) in two dimensions, with interaction potentials of the form (2), as encountered in numerical investigations of the associated particle system – cf. Section 2.4. The equilibria are placed in the (A, B)-plane according to their parameter values. For $(A, B) = (3, 3.5)$ and for $(A, B) = (3, 2)$ two distinct steady states are observed, depending on the initial data. Theoretical considerations using a variational approach and a linear analysis focus on the "overlap solution" seen here for $(A, B) = (0.5, 1)$ and the "target equilibrium" illustrated in the left-hand plot for $(A, B) = (3, 3.5)$.

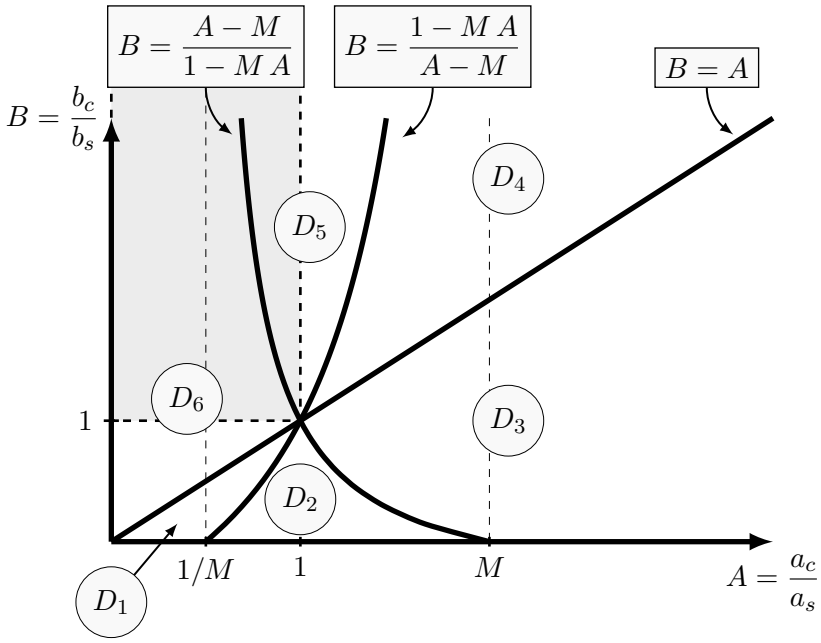

Figure 2: Regions of existence and stability of the equilibria; the solid lines are the regions' boundaries. The grey shaded area is the one where $A < 1$ and $B > 1$; for parameters in this region we identify *global* minimizers of the interaction energy.

ourselves to a subset of all possible perturbations, specifically to perturbations that are not entirely contained within the support of the equilibrium; throughout the paper we refer to such perturbations as perturbations of class $\mathcal{B}$ – see Section 2.2 for details. General perturbations (of compact support) could be dealt with only for $A < 1$ and $B > 1$, the shaded region in Figure 2.

Target equilibrium. In Section 3 we focus on a state in which the two species segregate and we have a disk of one species surrounded concentrically by an annular region of the other species. As noted above, we call such states targets. Target equilibria can be of two types, depending whether the lighter or the heavier species occupies the interior disk. A target equilibrium with the lighter (red diamonds) species inside is shown for $(A, B) = (3, 3.5)$, at the left-hand side, in Figure 1.

The main results concerning the two types of target equilibria are:

- Propositions 3.2 and 3.5 (local minimizers with respect to class $\mathcal{B}$ perturbations): The target equilibrium with the lighter species inside is a local minimizer with respect to perturbations of class $\mathcal{B}$ for (A, B) in $D_4 \cup D_5$, as well as for (A, B) in a certain subset of D_3. The target equilibrium with the heavier species inside is a local minimizer with respect to class $\mathcal{B}$ perturbations for all (A, B) in $D_2 \cup D_3$, and for (A, B) in a certain subset of D_4.

- Theorem 3.3 (global minimizer): The target equilibrium with the lighter species inside is a global minimizer with respect to compactly supported admissible densities, for all (A, B) in D_5 with $A < 1$, i.e., in the intersection of D_5 with the shaded region in Figure 2.

- Theorems 3.4 and 3.6: A target with the lighter species inside exists as a linearly stable steady state only in the parameter region $D_4 \cup D_5$. Whenever the target with the heavier species inside exists, it is unstable.

Note that due to the limitations of the variational approach, the predicted stability regions for both types of targets (light and heavy inside) in the variational study are larger compared to what the linear stability analysis and the numerics predict. Numerical investigations confirm the linear stability analysis: the target with the lighter species inside is only observed in $D_4 \cup D_5$, while the target with the heavier species inside is never encountered.

Overlap equilibrium. In Section 4 we investigate the state in which the supports of both species are two concentric disks of possibly different widths. Within the smallest of these disks, the two species coexist. We use the term "overlap" equilibria to refer to such configurations; an example of such a state is shown in Figure 1 for $(A, B) = (0.5, 1)$. In Section 4 only the variational approach is employed, as due to overlapping supports, perturbing boundaries to perform a linear stability, is very delicate.

We derive the following results on overlap equilibria:

- Propositions 4.1 and 4.3 (local minimizers with respect to class $\mathcal{B}$ perturbations): The overlap solution with the lighter species inside is a local minimizer with respect to class $\mathcal{B}$ perturbations for $(A, B) \in D_6$, but not for $(A, B) \in D_3$. The overlap solution with the heavier species inside is a local minimizer with respect to perturbations of class $\mathcal{B}$ when $(A, B) \in D_1$, but not for $(A, B) \in D_4$.

- Theorem 4.2 (global minimizer): The overlap equilibrium with the lighter species inside is a global minimizer with respect to admissible densities of compact support, for all (A, B) in D_6 with $B > 1$, i.e. in the intersection of D_6 with the shaded region in Figure 2.

The results on the overlap equilibria with the lighter species inside is in full agreement with what we find numerically. On the other hand, the overlap solution with the heavier species inside is never observed numerically. We conjecture that this overlap state is *not* in fact a minimizer for general perturbations.

Non-symmetric equilibria. In Section 3.3, we show by means of numerics how the non-radially symmetric states in the right-hand part of Figure 1, relate to the target solution. We

take parameters in certain regions where the target (either light, or heavy inside) is not a stable steady state. We initialize the system at the target (some small numerical deviation from the actual equilibrium being inevitably present), run the dynamics and wait until the small initial error triggers the instability. Some examples are illustrated in Figures 9 and 10. We relate this process with the mode instabilities found through linear analysis.

Similarly, the non-symmetric state shown for $(A, B) = (0.5, 0.4)$ arises by initializing the system in the overlap state. This is shown in Figure 13 of Section 4.3. Apparently, the two species' centres of mass coincide in D_6, yet the symmetry is broken once we cross the boundary $B = A$ and take parameters in D_1. The steady state for $(A, B) = (0.5, 0.4)$ exhibits in the middle an area in which the two species coexist. In Section 5 we quantify this process of radial symmetry breaking asymptotically in the limit of weak cross-interactions, that is, asymptotically close to $(A, B) = (0, 0)$. Asymptotically, as the strength of the cross-interactions goes to zero, we identify the following regimes (see Figure 15):

$A/B < 1$ **:** Both species fully mix and are supported on the same disk of radius $\sqrt{a_s/b_s}$.

$1 < A/B < 4$ **:** The two species partially mix, as they are supported on partially overlapping disks. The distance between the centres of mass is implicitly defined in terms of A/B.

$A/B = 4$ **:** The two species are supported on tangential disks.

$A/B > 4$ **:** The two species are supported on disjoint disks. The distance between the centres of mass increases proportionally to $\sqrt{A/B}$.

2 Preliminaries

In this section we present the two approaches taken in this paper to study the stability of equilibria, i.e., variational and linear analysis, along with some general properties of model (1). We refer specifically to the model in two dimensions, but the general properties and the variational formalism apply to any spatial dimension.

2.1 General preliminaries

The interaction potentials considered in this paper (see (2)) are symmetric, that is,

$$K_s(x) = K_s(-x), \qquad K_c(x) = K_c(-x), \qquad \text{for all } x. \tag{4}$$

Model (1) with symmetric interaction potentials conserves the mass and the centre of mass of each species, as elaborated below.

Conservation of mass and centre of mass. The dynamics of model (1) conserve the mass of each species:

$$\int \rho_i(x,t)\,\mathrm{d}x = M_i \qquad \text{for all } t \geq 0, \quad i = 1, 2, \tag{5}$$

as well as the total centre of mass:

$$\int x(\rho_1(x,t) + \rho_2(x,t))\,\mathrm{d}x = \text{ const.} \qquad \text{for all } t \geq 0. \tag{6}$$

Indeed, conservation of mass follows immediately as the equations of motion (1) are in conservation law form. To get (6), multiply each equation in (1) by x_k (x_k denotes the k-th spatial coordinate), and add the two equations. After integrating by parts and using vanishing at infinity boundary conditions, one finds

$$\frac{d}{dt}\int x_k(\rho_1(x,t) + \rho_2(x,t))\,dx = \int (\rho_1 v_1 + \rho_2 v_2)\cdot e_k\,dx, \tag{7}$$

where e_k denotes the unit vector in the direction of the k-th coordinate. Furthermore, by the expressions of v_1 and v_2 from (1a) and (1b), together with the symmetry of K_s, one gets

$$\int (\rho_1 v_1 + \rho_2 v_2)\,dx = -\underbrace{\iint \nabla K_s(x-y)\rho_1(x)\rho_1(y)\,dxdy}_{=0 \text{ by (4)}} - \iint \nabla K_c(x-y)\rho_1(x)\rho_2(y)\,dxdy$$
$$- \underbrace{\iint \nabla K_s(x-y)\rho_2(x)\rho_2(y)\,dxdy}_{=0 \text{ by (4)}} - \iint \nabla K_c(x-y)\rho_2(x)\rho_1(y)\,dxdy.$$

Finally, the symmetry of K_c yields the expression above zero, as

$$\iint \nabla K_c(x-y)(\rho_1(x)\rho_2(y)+\rho_2(x)\rho_1(y))\,dxdy = \iint (\underbrace{\nabla K_c(x-y) + \nabla K_c(y-x)}_{=0 \text{ by (4)}})\rho_1(x)\rho_2(y)\,dxdy.$$

From (7) one can now derive the conservation of centre of mass (6).

Equilibria for interaction potentials in the form (2)**.** Similar to the one-species model, interaction potentials in the form (2), have the outstanding property that they lead to equilibria of constant densities. Indeed, from the equation for v_1 in (1a), and (2), we get

$$\begin{aligned}\nabla \cdot v_1 &= -\Delta K_s * \rho_1 - \Delta K_c * \rho_2 \\ &= 2\pi a_s \rho_1 + 2\pi a_c \rho_2 - 2b_s M_1 - 2b_c M_2,\end{aligned} \tag{8}$$

where for the second equality we also used $\Delta\left(\frac{1}{2\pi}\ln|x|\right) = \delta$, and the mass constraint (5). Also, by a similar calculation,

$$\nabla \cdot v_2 = 2\pi a_s \rho_2 + 2\pi a_c \rho_1 - 2b_s M_2 - 2b_c M_1. \tag{9}$$

Note that due to the specific form of the interaction potentials used here, $\nabla \cdot v_i$ are *local* quantities, i.e., $\nabla \cdot v_i(x)$ depends only on the values of the densities $\rho_1(x)$ and $\rho_2(x)$ at location x. As seen below, the key consequence of this fact is that at equilibrium, the two species must have constant densities on their supports.

Consider now an equilibrium configuration $(\bar\rho_1, \bar\rho_2)$ for model (1) with interaction potentials given by (2). At any point x in the support of $\bar\rho_i$, the velocity $\bar v_i$ (and consequently its divergence) vanishes. Hence, at a point x that lies in the supports of *both* $\bar\rho_1$ and $\bar\rho_2$ (i.e., where the two species overlap), by (8) and (9), the values of the equilibrium densities $\bar\rho_1(x)$ and $\bar\rho_2(x)$ satisfy a linear system of equations – see its solution in (10) below. On the other hand, if x lies in the support of species i, but outside the support of species j (here $j \neq i$), then $\bar\rho_j(x) = 0$ and by setting $\nabla \cdot \bar v_i(x)$ to 0 (use (8) if $i = 1$ or (9) if $i = 2$) one finds an explicit expression for $\bar\rho_i(x)$. Finally, there is the trivial case in which x is not in the support of either species, in which case $\bar\rho_i(x) = 0$ $(i = 1, 2)$.

To conclude, by the considerations above, there are four possible combinations that the equilibrium densities of the two species can have at location x:

$$(\bar\rho_1(x), \bar\rho_2(x)) = \begin{cases} (0,0), & \text{for } x \notin \operatorname{supp}(\bar\rho_1) \cup \operatorname{supp}(\bar\rho_2) \\ \left(0, \frac{b_c M_1 + b_s M_2}{\pi a_s}\right), & \text{for } x \notin \operatorname{supp}(\bar\rho_1), x \in \operatorname{supp}(\bar\rho_2) \\ \left(\frac{b_s M_1 + b_c M_2}{\pi a_s}, 0\right), & \text{for } x \in \operatorname{supp}(\bar\rho_1), x \notin \operatorname{supp}(\bar\rho_2) \\ \left(\frac{(a_s b_s - a_c b_c)M_1 + (a_s b_c - a_c b_s)M_2}{\pi(a_s^2 - a_c^2)}, \quad \frac{(a_s b_c - a_c b_s)M_1 + (a_s b_s - a_c b_c)M_2}{\pi(a_s^2 - a_c^2)}\right), & \\ & \text{for } x \in \operatorname{supp}(\bar\rho_1) \cap \operatorname{supp}(\bar\rho_2). \end{cases} \tag{10}$$

We use the parameters A and B introduced in (3), to define the (A, B) phase plane. This phase plane is given in Figure 2 and subdivided in six regions named D_1 to D_6. The exact formulas for the boundaries of these regions are a result of our investigation of the existence and stability of steady states. More details will be given in Sections 3 and 4. The same phase plane was already used in Figure 1 to present the gallery of numerical steady states. Note that in each equilibrium configuration shown in Figure 1 the two species have constant densities within their supports, regardless of whether the equilibria are radially symmetric or not.

2.2 Variational approach

Energy and gradient flow. The interaction energy corresponding to model (1) is given by

$$E[\rho_1, \rho_2] = \frac{1}{2} \iint K_s(x-y) \left(\rho_1(x)\rho_1(y) + \rho_2(x)\rho_2(y)\right) \mathrm{d}x \, \mathrm{d}y + \iint K_c(x-y)\rho_1(x)\rho_2(y) \, \mathrm{d}x \, \mathrm{d}y, \tag{11}$$

where the two terms represent the self-interaction and the cross-interaction energies, respectively. While there has been significant progress recently on the study of minimizers for the interaction energy of the one-species model [2, 5, 12, 16, 12, 39], there is only a handful of works on the two-species interaction energy.

In [21] the authors make precise the gradient flow structure (with respect to energy (11)) of model (1) by generalizing the theory of gradient flows on probability spaces previously developed for the one-species model [13]. The setup there is very general and allows for measure-valued solutions and mildly singular (C^1 except at origin) interaction potentials. Studying critical points and minimizers of the energy functional (11) is central to our variational approach. We also point out that there are related works on ground states for two-phase/two-species interaction energies such as (11), where interactions are assumed to be purely attractive, but with an additional requirement of boundedness being enforced [17, 4]. In [4] the setting of [17] is extended by including diffusion (entropy). Moreover, they study the connection between energy minimizers and the long-time dynamics of the gradient flow.

General variational setup. The authors in [5] study the energy functional that corresponds to the one species model and find conditions for critical points to be energy minimizers. We adapt the setup from there to the two species model. We note here that, while the extension to multiple species is immediate, it does not appear explicitly anywhere in literature. For this reason, we lay out first the variational framework for generic interaction potentials K_s and K_c, before using it for the specific potentials in (2).

By conservation properties (5) and (6), we consider the variational problem of minimizing $E[\rho_1, \rho_2]$ from (11) over densities that have fixed masses and total centre of mass (also note here that the energy E is translation invariant). Hence, with no loss of generality we can take the centre of mass of admissible densities to be at the origin. The variational problem is to minimize E over the set $\mathcal{F}$ given by

$$\mathcal{F} = \left\{ (\rho_1, \rho_2) \middle| \ \rho_i : \mathbb{R}^2 \to [0, \infty), \int_{\mathbb{R}^2} \rho_i(x) dx = M_i, \int_{\mathbb{R}^2} x(\rho_1(x) + \rho_2(x)) \, \mathrm{d}x = 0 \right\}. \tag{12}$$

Consider $(\bar{\rho}_1, \bar{\rho}_2) \in \mathcal{F}$ with masses (M_1, M_2) and supports (Ω_1, Ω_2), and take a small perturbation $\varepsilon(\tilde{\rho}_1, \tilde{\rho}_2)$:

$$\rho_i(x) = \bar{\rho}_i(x) + \varepsilon \tilde{\rho}_i(x), \qquad i = 1, 2, \tag{13}$$

where $(\rho_1, \rho_2) \in \mathcal{F}$. Perturbations are assumed to preserve the individual masses of the two species, as well as the total centre of mass, i.e., they satisfy:

$$\int_{\mathbb{R}^2} \tilde{\rho}_i(x) \, \mathrm{d}x = 0, \qquad i = 1, 2, \tag{14}$$

and

$$\int_{\mathbb{R}^2} x(\tilde{\rho}_1(x) + \tilde{\rho}_2(x))\,\mathrm{d}x = 0. \tag{15}$$

Since the energy functional is quadratic, one can write:

$$E[\rho_1, \rho_2] = E[\bar{\rho}_1, \bar{\rho}_2] + \varepsilon E_1[\bar{\rho}_1, \bar{\rho}_2, \tilde{\rho}_1, \tilde{\rho}_2] + \varepsilon^2 E_2[\tilde{\rho}_1, \tilde{\rho}_2], \tag{16}$$

where E_1 denotes the first variation:

$$\begin{aligned} E_1[\bar{\rho}_1, \bar{\rho}_2, \tilde{\rho}_1, \tilde{\rho}_2] = &\int \left[\int K_s(x-y)\bar{\rho}_1(y)\,\mathrm{d}y + \int K_c(x-y)\bar{\rho}_2(y)\,\mathrm{d}y \right] \tilde{\rho}_1(x)\,\mathrm{d}x \\ &+ \int \left[\int K_s(x-y)\bar{\rho}_2(y)\,\mathrm{d}y + \int K_c(x-y)\bar{\rho}_1(y)\,\mathrm{d}y \right] \tilde{\rho}_2(x)\,\mathrm{d}x, \end{aligned} \tag{17}$$

and E_2 the second variation, which in fact has the same expression as the energy itself:

$$E_2[\tilde{\rho}_1, \tilde{\rho}_2] = E[\tilde{\rho}_1, \tilde{\rho}_2]. \tag{18}$$

In the sequel, we will consider two classes of perturbations, denoted as $\mathcal{A}$ and $\mathcal{B}$. These choices are inspired by the setup in [5]. Class $\mathcal{A}$ consists of perturbations $(\tilde{\rho}_1, \tilde{\rho}_2)$ such that each $\tilde{\rho}_i$ is supported in Ω_i (here $i = 1, 2$). Class $\mathcal{B}$ is made of perturbations $(\tilde{\rho}_1, \tilde{\rho}_2)$ such that at least one $\tilde{\rho}_i$ has a support with a non-empty intersection with the complement Ω_i^c of Ω_i $(i = 1, 2)$. By considering class $\mathcal{A}$ perturbations, one can test whether an equilibrium is an energy minimizer with respect to redistributions of mass of species i within its own support Ω_i. Similarly, by considering class $\mathcal{B}$ perturbations one checks whether transporting mass from Ω_i into its complement Ω_i^c results (or not) into a more energetically favourable state. Hence, $\mathcal{A}$ and $\mathcal{B}$ are disjoint and cover all possible perturbations $(\tilde{\rho}_1, \tilde{\rho}_2)$.

Start by taking perturbations of class $\mathcal{A}$. Since $\tilde{\rho}_i$ changes sign in Ω_i $(i = 1, 2)$, for $(\bar{\rho}_1, \bar{\rho}_2)$ to be a critical point of the energy, the first variation must vanish. Using the notations

$$\Lambda_1(x) = \int_{\Omega_1} K_s(x-y)\bar{\rho}_1(y)\,\mathrm{d}y + \int_{\Omega_2} K_c(x-y)\bar{\rho}_2(y)\,\mathrm{d}y, \tag{19a}$$

$$\Lambda_2(x) = \int_{\Omega_2} K_s(x-y)\bar{\rho}_2(y)\,\mathrm{d}y + \int_{\Omega_1} K_c(x-y)\bar{\rho}_1(y)\,\mathrm{d}y,, \tag{19b}$$

in (17), one can write the first variation as

$$E_1[\bar{\rho}_1, \bar{\rho}_2, \tilde{\rho}_1, \tilde{\rho}_2] = \int_{\mathbb{R}^2} \Lambda_1(x)\tilde{\rho}_1(x)\,\mathrm{d}x + \int_{\mathbb{R}^2} \Lambda_2(x)\tilde{\rho}_2(x)\,\mathrm{d}x. \tag{20}$$

Then, given that perturbations $\tilde{\rho}_i$ are arbitrary and satisfy (14), one finds that E_1 vanishes provided Λ_i is constant a.e. in Ω_i, i.e.,

$$\Lambda_1(x) = \lambda_1 \quad \text{for } a.e.\ x \in \Omega_1, \quad \text{and} \quad \Lambda_2(x) = \lambda_2 \quad \text{for } a.e.\ x \in \Omega_2. \tag{21}$$

The above conditions can also be found via a Lagrange multiplier argument, by imposing the constant mass condition as a constraint [5]. Also, cf. [5], $\Lambda_i(x)$ has a physical interpretation: it represents the energy per unit mass felt by a test mass of species i at position x, due to interaction with the swarm. At equilibrium, this energy is constant within each species.

Equation (21) represents a necessary condition for $(\bar{\rho}_1, \bar{\rho}_2)$ to be an equilibrium. For $(\bar{\rho}_1, \bar{\rho}_2)$ that satisfy (21) to be a local minimizer with respect to class $\mathcal{A}$ perturbations, the second variation (18) must be non-negative. In general, the sign of E_2 cannot be assessed easily.

Consider now perturbations of class $\mathcal{B}$. Since perturbations $\tilde{\rho}_i$ must be non-negative in the complement Ω_i^c of Ω_i, one can extend the argument in [5] and show that a necessary and sufficient condition for $E_1 \geq 0$ is

$$\Lambda_1(x) \geq \lambda_1 \quad \text{for } a.e.\ x \in \Omega_1^c, \quad \text{and} \quad \Lambda_2(x) \geq \lambda_2 \quad \text{for } a.e.\ x \in \Omega_2^c. \tag{22}$$

Given the physical interpretation of $\Lambda_i(x)$ as energy (per unit mass), (22) assures that transporting mass from Ω_i into its complement Ω_i^c increases the total energy [5].

To show that (22) is sufficient for $E_1 \geq 0$, suppose an equilibrium $(\bar{\rho}_1, \bar{\rho}_2)$ satisfies (21) and (22). Then,

$$\begin{aligned} E_1 &= \int_{\Omega_1} \underbrace{\Lambda_1(x)}_{=\lambda_1} \tilde{\rho}_1(x)\,\mathrm{d}x + \int_{\Omega_1^c} \underbrace{\Lambda_1(x)}_{\geq\lambda_1} \tilde{\rho}_1(x)\,\mathrm{d}x + \int_{\Omega_2} \underbrace{\Lambda_2(x)}_{=\lambda_2} \tilde{\rho}_2(x)\,\mathrm{d}x + \int_{\Omega_2^c} \underbrace{\Lambda_2(x)}_{\geq\lambda_2} \tilde{\rho}_2(x)\,\mathrm{d}x \\ &\geq \lambda_1 \int_{\mathbb{R}^2} \tilde{\rho}_1(x)\,\mathrm{d}x + \lambda_2 \int_{\mathbb{R}^2} \tilde{\rho}_2(x)\,\mathrm{d}x, \end{aligned}$$

where we also used that $\tilde{\rho}_i \geq 0$ in Ω_i^c. By (14) one concludes $E_1 \geq 0$.

Conversely, suppose that (22) does not hold; assume for instance that $\Lambda_1(x) < \lambda_1$, for x in a set $A \subset \Omega_1^c$ of non-zero Lebesgue measure. Then, by taking $\tilde{\rho}_2 = 0$ and perturbations $\tilde{\rho}_1$ that are supported on Ω_1 and A, we have

$$E_1 = \int_{\Omega_1} \underbrace{\Lambda_1(x)}_{=\lambda_1} \tilde{\rho}_1(x)\,\mathrm{d}x + \int_{A} \underbrace{\Lambda_1(x)}_{<\lambda_1} \tilde{\rho}_1(x)\,\mathrm{d}x.$$

Again, by (14), one finds $E_1 < 0$, which completes the argument.

In summary, a critical point $(\bar{\rho}_1, \bar{\rho}_2)$ for the energy satisfies the Fredholm integral equation (21) on its support. The critical point is a local minimum with respect to perturbations of class $\mathcal{A}$ if the second variation is non-negative for such perturbations. Also, $(\bar{\rho}_1, \bar{\rho}_2)$ is a local minimizer with respect to perturbations of class $\mathcal{B}$ if it satisfies (22).

To establish whether an equilibrium is a global minimizer, one needs to investigate closely the second variation E_2 for general perturbations. From (16) we see that a sufficient condition for a local minimizer to be global minimizer is that $E_2 \geq 0$. Such condition is not necessary though, as (16) is exact, and for a global minimum one needs in fact $\varepsilon E_1 + \varepsilon^2 E_2 \geq 0$, for arbitrary $\varepsilon > 0$.

Remark 2.1. *We note that in the minimization considerations above we followed the simplified setup and approach from [5]. A reader interested in a mathematically complete and rigorous framework of the minimization conditions* (22) *(including a rigorous derivation of the Euler-Lagrange equations* (21)*) can consult for instance [2, Theorem 4]; the derivation there is for equilibria of one species in free space, but it extends immediately to multiple species and arbitrary domains Ω, as considered in this paper. The authors in [2] consider the variational problem over more general admissible densities that lie in a Borel measure space, endowed with the 2-Wasserstein metric [2, 3]. In fact, we could have also worked in a more general setup and consider minimization over measure spaces (as opposed to over integrable non-negative densities as in* (12)*), but given the equilibria that we are investigating in this work, adding such technicalities into our study would have obstructed the presentation.*

Throughout the paper we apply the variational framework above for interaction potentials given by (2) and equilibria consisting of target and overlap configurations. For such specific choices, exact expressions for $\Lambda_1(s)$ and $\Lambda_2(x)$ can be found and consequently, minimization with respect to class $\mathcal{B}$ perturbations (cf. (22)) be investigated explicitly. A more challenging task is to assess the sign of the second variation E_2, and hence draw conclusions with respect to class $\mathcal{A}$ perturbations. We have some partial results in this regard, based on an explicit calculation of E_2 (corresponding to potentials (2)); we present below this calculation.

Second variation E_2 for interaction potentials of form (2)**.** A challenging aspect in the variational study is to establish the sign of the second variation of the energy. Assessing the sign of E_2 is needed if one wants to determine whether an equilibrium $(\bar{\rho}_1, \bar{\rho}_2)$ is a local minimizer with respect to class $\mathcal{A}$ perturbations. Also, given that formula (16) is *exact*, by determining

the sign of the second variation one can establish whether an equilibrium is a *global* minimizer, as detailed below.

Consider the second variation of the energy E_2 that corresponds to the interaction potentials (2). By (18) and (11), we can write

$$E_2(\tilde{\rho}_1, \tilde{\rho}_2) = I + II, \tag{23}$$

where

$$I := -\frac{1}{2}a_s \iint \ln|x-y|(\tilde{\rho}_1(x)\tilde{\rho}_1(y) + \tilde{\rho}_2(x)\tilde{\rho}_2(y))\,dxdy - a_c \iint \ln|x-y|\tilde{\rho}_1(x)\tilde{\rho}_2(y)\,dxdy,$$
$$II := \frac{1}{4}b_s \iint |x-y|^2(\tilde{\rho}_1(x)\tilde{\rho}_1(y) + \tilde{\rho}_2(x)\tilde{\rho}_2(y))\,dxdy + \frac{1}{2}b_c \iint |x-y|^2\tilde{\rho}_1(x)\tilde{\rho}_2(y)\,dxdy.$$

We will pursue the following strategy. The expression for term II can be easily simplified by expanding $|x-y|^2$ and using the conservation properties (14) and (15) of the perturbations. Term I is more subtle, as integrals there involve the logarithmic potential, which becomes infinite at origin (where it is integrable however), as well as at infinity. For this reason, in the study on E_2 that follows below we consider the variational problem on densities in $\mathcal{F}$ that are compactly supported:

$$\mathcal{F}_c = \{(\rho_1, \rho_2) \in \mathcal{F},\ \rho_i \text{ has compact support in } \mathbb{R}^2\}. \tag{24}$$

Note that by restricting to densities in $\mathcal{F}_c$, the admissible perturbations $\tilde{\rho}_1, \tilde{\rho}_2$ are also compactly supported in $\mathbb{R}^2$.

For term II above, one finds by expanding $|x-y|^2 = |x|^2 - 2x\cdot y + |y|^2$ and using (14) and (15):

$$\begin{aligned} II &= -\frac{1}{2}b_s\left(\int x\tilde{\rho}_1(x)\,dx\right)^2 - \frac{1}{2}b_s\left(\int x\tilde{\rho}_2(x)\,dx\right)^2 - b_c\left(\int x\tilde{\rho}_1(x)\,dx\right)\left(\int x\tilde{\rho}_2(x)\,dx\right) \\ &= (b_c - b_s)\left(\int x\tilde{\rho}_1(x)\,dx\right)^2. \end{aligned} \tag{25}$$

For term I we use the theory for logarithmic potentials presented in [35]. Theorem 1.16 in [35, Chapter I] states that the symmetric bilinear form

$$-\iint_{\mathbb{R}^2\times\mathbb{R}^2} \ln|x-y|\,d\mu(x)\,d\nu(y)$$

is positive definite on the space of signed measures with compact support in $\mathbb{R}^2$ that satisfy $\int d\mu(x) = 0$. In other words, the bilinear form above is an inner product.

Given the $\tilde{\rho}_i$ are compactly supported and integrate to zero (by (14)), $\tilde{\rho}_i\,dx$ belong to this inner product space and by Cauchy-Schwarz inequality,

$$\left|\iint \ln|x-y|\tilde{\rho}_1(x)\tilde{\rho}_2(y)\,dxdy\right| \leq \left(-\iint \ln|x-y|\tilde{\rho}_1(x)\tilde{\rho}_1(y)\,dxdy\right)^{\frac{1}{2}}\left(-\iint \ln|x-y|\tilde{\rho}_2(x)\tilde{\rho}_2(y)\,dxdy\right)^{\frac{1}{2}}.$$

Then, one can estimate

$$I \geq \frac{1}{2}(a_s - a_c)\left(-\iint \ln|x-y|\tilde{\rho}_1(x)\tilde{\rho}_1(y)\,dxdy - \iint \ln|x-y|\tilde{\rho}_2(x)\tilde{\rho}_2(y)\,dxdy\right), \tag{26}$$

where the term in the round brackets on the right-hand-side is non-negative.

We also note here that an alternative way for investigating term I is to use the Fourier transform and Plancherel's theorem; one has to use in this case that $\frac{1}{2\pi}\ln|x|$ is the Green's

function of the Laplacian in two dimensions, with Fourier symbol $\frac{1}{2\pi}\widehat{\ln|x|}(k) = -\frac{1}{|k|^2}$. Bounding the cross term (the inner product) by Cauchy-Schwarz would follow similarly and one can reach a Fourier space analogue of (26).

Given that the expression (16) for energy is exact, the considerations above lead to some immediate conclusions. Consider parameters such that $a_s > a_c$ and $b_c > b_s$ ($A < 1$ and $B > 1$; the shaded region in Figure 2) and a corresponding equilibrium configuration $(\bar{\rho}_1, \bar{\rho}_2) \in \mathcal{F}_c$. In particular, $(\bar{\rho}_1, \bar{\rho}_2)$ can be either the target or the overlap equilibrium with the lighter species inside, as found to the right and to the left of the curve $B = \frac{A-M}{1-MA}$, respectively – see Figure 1. Assume further that $(\bar{\rho}_1, \bar{\rho}_2)$ is a local minimizer with respect to perturbations of class $\mathcal{B}$ (i.e., it satisfies (22)). Take now an arbitrary, *compactly supported* perturbation $(\tilde{\rho}_1, \tilde{\rho}_2)$; by the local minimizer condition, one has $E_1 \geq 0$. Furthermore, by (23), (25) and (26) above, we have $E_2[\tilde{\rho}_1, \tilde{\rho}_2] \geq 0$. This implies that the equilibrium under consideration is in fact a *global* minimizer in $\mathcal{F}_c$ (see Theorems 3.3 and 4.2 on how this observation is applied to the target and the overlap equilibria with the lighter species inside).

For values of the parameters outside $A < 1$ and $B > 1$, establishing the sign of the second variation is a challenging task. The reason lies in the very different expressions of the terms I and II that comprise E_2; the two terms are not immediately comparable and also, the logarithmic potential is not sign-definite. Balancing term I and II to yield a definite sign for E_2 seems difficult and we do not pursue this direction here. The best we can do in such regimes, using the variational method above, is to check for the sign of E_1 (condition (22)) and restrict our conclusions to local minimizers with respect to perturbations of class $\mathcal{B}$.

To conclude, unless $A < 1$ and $B > 1$, we only establish in this paper, by the variational approach, whether a specific equilibrium is a local minimizer with respect to perturbations of class $\mathcal{B}$. We do not make any conclusion concerning minimization with respect to class $\mathcal{A}$ perturbations. To compensate for this limitation, we develop and use an alternative approach for studying the stability of equilibria, based on linear analysis. We present now the main features of this alternative approach.

2.3 Linear stability analysis

Class of perturbations and difference with variational approach. In (10) we identified the values that the density can attain in a steady state. In particular, any steady state consists of regions where (a) only one of the species has nonzero density, (b) the two species coexist, or (c) none of the species is present. Within each of these subdomains, the density of each species is a constant given by (10).

These properties of steady states are a specific consequence of the choice of potentials in (2). The fact that the steady states are piecewise constant, makes us consider here perturbations in which the densities remain constant, but the boundaries of the supports are deformed; cf. [15]. We consider deformations such that the total area enclosed remains unchanged (up to higher-order contributions), due to the constraint of fixed total mass.

The perturbations considered here are completely different in spirit from the ones used in the variational approach. The difference lies in the meaning of the word 'small', when we speak about 'small perturbations'. Here, 'small' means that only *close* to the boundaries of the supports, the density may change. That is, exactly at those points that were outside the support of the unperturbed equilibrium, but now fall within the support of the perturbed state (upon alteration of the boundaries), or *vice versa*. The change in density is $\mathcal{O}(1)$ at those points, according to the discrete set of values allowed by (10). In the variational approach, perturbations change the value of the density only *slightly* (cf. multiplication by ε in (13)), but on the other hand, are allowed to be *nonlocal* in space (in particular, not necessarily close to the equilibrium's support).

Mathematical description for a single species. To explain the essence of the method, we will first consider the model for a single species so that we can avert some of the technicalities

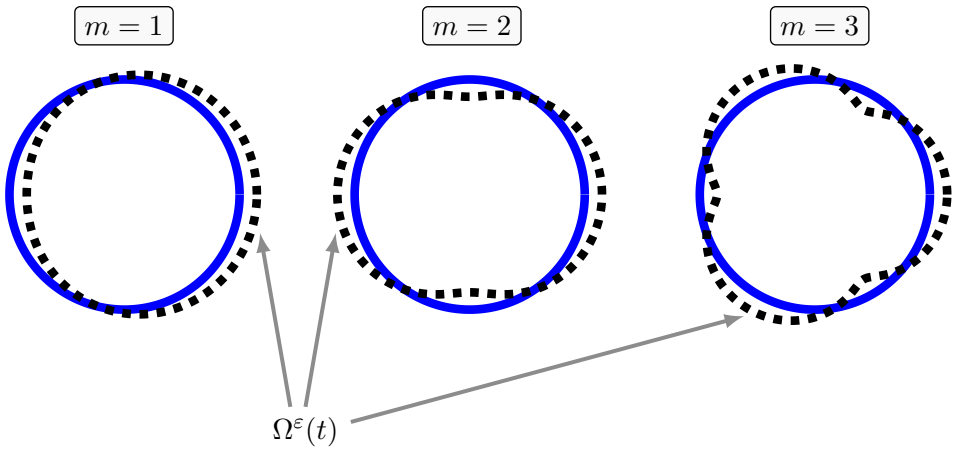

Figure 3: Schematic drawing of the perturbations for modes $m = 1$, $m = 2$ and $m = 3$. The unperturbed circular boundary is given in blue. The perturbed boundary $\Omega^\varepsilon(t)$ is indicated by the dashed line. Node that the mode m is also an indication of the number of oscillations.

that arise for two species. In the single species model, the density is denoted by ρ and the velocity is given by

$$v = -\nabla K * \rho, \qquad \text{with} \qquad K(x) = -a \ln|x| + \frac{b}{2}|x|^2, \tag{27}$$

where $a, b \geqslant 0$ are interaction parameters that correspond to repulsion and attraction, respectively. For one species it is known [7, 26] that there is a steady state of constant density $\bar{\rho} := \bar{M}\, b/(\pi\, a)$ supported on a disk of radius $R := \sqrt{a/b}$. This steady state is in fact a global attractor. Here, $\bar{M} := \int \rho(x,t)\, dx$ is the total mass that is constant in time.

For mathematical convenience, we identify the domain $\mathbb{R}^2$ with the complex plane. We will now consider small perturbations of the boundary of the support $B(0,R)$ and investigate how the boundary evolves in time. Similarly to [33], we consider the following perturbations (corresponding to Fourier mode $m \in \mathbb{N}^+$):

$$p(\theta,t) := R\, e^{i\,\theta}\,(1 + \varepsilon_N(t)\, \cos(m\,\theta) + i\,\varepsilon_T(t)\, \sin(m\,\theta))\,, \qquad \text{for } 0 \leqslant \theta < 2\pi, \tag{28}$$

where $\varepsilon_N(t)$ and $\varepsilon_T(t)$ are assumed to have small amplitude; they control the normal ('N') and transversal ('T') deformation.

Let $\Omega^\varepsilon(t)$ denote the perturbed domain enclosed by $p(\theta,t)$; note that it depends on m. Roughly speaking, due to perturbations (28), a number of "oscillations" are superimposed on the unperturbed circular boundary. The number of oscillations is determined by the mode m. An illustration for the first three modes is given in Figure 3. Here we have in mind the idea that any *arbitrary* perturbation can be obtained by using its decomposition in Fourier modes (28). Note that in the sequel, we will mostly omit to indicate explicitly the time dependence of p, ε_N, ε_T and Ω^ε.

The area of Ω^ε is $\pi R^2 + \frac{1}{2}\pi R^2(\varepsilon_N^2 + \varepsilon_T^2)$, independent of the mode m. For $m \geqslant 2$, the perturbations in (28) preserve the centre of mass. For $m = 1$, we have that

$$\int_{\Omega^\varepsilon} y\, dy = \pi R^3 \varepsilon_N + \frac{1}{4}\pi R^3(\varepsilon_N^2 - \varepsilon_T^2)(\varepsilon_N + \varepsilon_T).$$

Recall that in this approach we consider perturbations from equilibrium such that the density remains constant (value $\bar{\rho}$) within the perturbed domain. To assess the stability, we investigate the dynamics of a generic point on the perturbed boundary. Such a point we label by its angle $0 \leqslant \theta_0 < 2\pi$, and its evolution satisfies

$$\frac{d}{dt} p(\theta_0, t) = v\big(p(\theta_0,t),t\big). \tag{29}$$

It follows from (28) that

$$\frac{d}{dt}p(\theta_0,t) = R\,e^{i\,\theta_0}\left(\varepsilon_N'(t)\,\cos(m\,\theta_0) + i\,\varepsilon_T'(t)\,\sin(m\,\theta_0)\right). \tag{30}$$

For the specific potential in (27) it is possible to find an explicit expression for the linearized right-hand side of (29). One finds that the $\mathcal{O}(1)$ terms vanish; this is a necessary condition for a steady state. The ansatz (28) turns out to be self-consistent: we can divide the linearized equation by $R\exp(i\,\theta_0)$ and match sine and cosine terms on both sides, to obtain a θ_0-independent system of the form

$$\frac{d}{dt}\begin{bmatrix}\varepsilon_N\\ \varepsilon_T\end{bmatrix} = Q_m\begin{bmatrix}\varepsilon_N\\ \varepsilon_T\end{bmatrix}, \tag{31}$$

where Q_m is a 2×2 matrix that depends on the mode m. The eigenvalues of Q_m are the growth/decay rates of the perturbations, and negative eigenvalues of Q_m indicate that the state under consideration is stable for that particular mode m.

For the case of a single species, we will now obtain the matrices Q_m ($m=1,2,\ldots$) and inspect their eigenvalues. We first need to obtain the velocity given in (27) at position $x=p(\theta_0,t)$, and thus we need to evaluate the convolution integral of $-\nabla K$ against the density, that is constant $\bar\rho$ inside the support $\Omega^\varepsilon(t)$. As the density is assumed to remain constant, one can take $\bar\rho$ outside the integral sign; consequently, to find the velocity at $x\in\mathbb{R}^2$ one has to evaluate

$$\int_{\Omega^\varepsilon(t)} \nabla K(x-y)\,dy. \tag{32}$$

By some abuse of notation, we used $\Omega^\varepsilon(t)\subset\mathbb{C}$ for the integration domain in $\mathbb{R}^2$. Note that the function $v(\cdot,t)$ in (29) depends itself on t because the domain of integration $\Omega^\varepsilon(t)$ in (32) is time-dependent.

Due to the choice of potential in (27), the integral (32) can be written as a linear combination of

$$\int_{\Omega^\varepsilon}\frac{x-y}{|x-y|^2}\,dy, \qquad \text{and} \qquad \int_{\Omega^\varepsilon}(x-y)\,dy. \tag{33}$$

The latter integral is relatively easy to evaluate exactly, using the aforementioned expressions for the area and centre of mass of Ω^ε. The outcome is given in (92) of Appendix B, where higher-order terms are omitted.[2] We emphasize that the specific choice $x=p(\theta_0,t)$ introduces a dependence on ε_N and ε_T as well.

By Gauss' theorem, the left-hand integral in (33) can be transformed into a contour integral over the boundary $\partial\Omega^\varepsilon$. We have

$$\int_{\Omega^\varepsilon}\frac{x-y}{|x-y|^2}\,dy = -\int_{\partial\Omega^\varepsilon}\ln|x-y|\,\hat n\,dS, \tag{34}$$

where we used that $(x-y)/|x-y|^2 = -\nabla_y\ln|x-y|$. The boundary of $\Omega^\varepsilon(t)$ is parameterized by $p(\theta,t)$, for $0\leqslant\theta<2\pi$. Consequently, $\hat n\,dS$ can be expressed in terms of θ, ε_N and ε_T; see (93) in Appendix B.[2]

The resulting one-dimensional integral (see (94) in Appendix B) depends in a nonlinear way on the small parameters ε_N and ε_T through the integration contour $\partial\Omega^\varepsilon$ and the fact that $x=p(\theta,t)$. In our linear stability analysis, we expand the integrand in terms of the small parameters, we omit higher-order terms and end up with integrals that can be evaluated. See Appendix B for more details. The first-order approximation of (34) is given in (102).[2]

After dividing the linearized equation by $R\exp(i\,\theta_0)$ and matching sine and cosine terms, we finally find the system (31) with

$$Q_1 = \begin{bmatrix}0 & 0\\ 0 & 0\end{bmatrix}, \quad \text{and} \quad Q_m = \begin{bmatrix}-b\,\bar M & 0\\ b\,\bar M & 0\end{bmatrix} \quad \text{when } m\geqslant 2.$$

[2]At this stage, the reader should simply disregard the indices j and ℓ that appear in Appendix B.

For every $m \geqslant 1$ the matrix Q_m has an eigenvalue 0 with eigenvector $(0,1)^T$. The corresponding solution of (31) is $(\varepsilon_N(t), \varepsilon_T(t))^T = (0,1)^T \cdot \exp(0 \cdot t) \equiv (0,1)^T$. This reflects a tangential perturbation of the boundary which –to leading order– does not influence the shape. Mode $m = 1$ has another eigenvalue 0, which corresponds to eigenvector $(1,-1)^T$. The associated (constant) solution of (31) is $(\varepsilon_N(t), \varepsilon_T(t))^T = (1,-1)^T \cdot \exp(0 \cdot t) \equiv (1,-1)^T$ and describes for $m = 1$ a translation of the curve (28). The system is invariant under translations since it conserves the centre of mass. For $m \geqslant 2$ the remaining eigenvalue $-b\,\bar{M}$ is negative, implying stability.

Two species and target states. Let us now outline the method for two species. In Figure 1 we identified several steady states numerically, among which is the one we called the 'target' (see also equilibria shown schematically in Figures 4 and 8). We will apply the linear stability analysis to such equilibrium states. A short explanation of why we only consider these states follows at the end of this section.

For a target, there are three circles of different radii that form the boundaries of the supports. Each of these circles is perturbed to a time-dependent curve similar to (28):

$$p_j(\theta,t) := R_j\, e^{i\,\theta}\,(1 + \varepsilon_{j,N}(t)\,\cos(m\,\theta) + i\,\varepsilon_{j,T}(t)\,\sin(m\,\theta))\,, \qquad \text{for } 0 \leqslant \theta < 2\pi, \tag{35}$$

where $j \in \{0,1,2\}$, and where $\varepsilon_{j,N}(t)$ and $\varepsilon_{j,T}(t)$ are assumed to have small amplitude. We use the notation $\Omega_j^\varepsilon(t)$ for the perturbed domain enclosed by $p_j(\theta,t)$; each of these domains looks like the ones presented in Figure 3.

By assumption the densities are constant inside the supports (values $\bar{\rho}_1$ and $\bar{\rho}_2$). Consequently, the velocity at x becomes a weighted sum over $\ell \in \{0,1,2\}$ of integrals of the type

$$\int_{\Omega_\ell^\varepsilon(t)} \nabla K(x-y)\,dy. \tag{36}$$

Note for instance, that the integral over the (perturbed) annulus in the target state is obtained by subtracting integrals like these, for two different values of ℓ. The potential K in (36) either denotes K_s or K_c. Due to the choice of these potentials in (2), the integral (36) can be written in terms of

$$\int_{\Omega_\ell^\varepsilon} \frac{x-y}{|x-y|^2}\,dy = -\int_{\partial\Omega_\ell^\varepsilon} \ln|x-y|\,\hat{n}\,dS, \qquad \text{and} \qquad \int_{\Omega_\ell^\varepsilon} (x-y)\,dy. \tag{37}$$

To assess the stability of the configuration, we take a generic point on each of the three boundaries, that is, we let $x = p_j(\theta_0,t)$, with $j = 0$, $j = 1$ or $j = 2$. At each of these points, we compute and linearize the velocity, combining contributions of the form (37). The constants in front of the terms depend on $\bar{\rho}_1$, $\bar{\rho}_2$, a_s, a_c, b_s and b_c, and the exact details are configuration-specific. These details are given in Sections 3.1.2 and 3.2.2.

Similarly to the exposition for a single species, we can find precise first-order expressions for the integrals in (37); the results are presented in Appendix B. We remark that for the left-hand integral in (37) the expression depends on whether $x = p_j(\theta_0,t)$ is inside, on or outside $\partial\Omega_\ell^\varepsilon(t)$.

Let $\underline{\varepsilon}(t)$ be the vector of six components formed with $\varepsilon_{j,N}(t)$, $\varepsilon_{j,T}(t)$, with $j = 0,1,2$. Similarly to the single species case, from the system of linearized equations for $\frac{d}{dt}p_j(\theta_0,t)$ we can deduce for each $m \in \mathbb{N}^+$ a system of the form

$$\frac{d}{dt}\underline{\varepsilon} = Q_m\,\underline{\varepsilon}, \tag{38}$$

where Q_m is a 6×6 matrix. The system (38) gives the evolution of $\underline{\varepsilon}(t)$ to leading order, and the eigenvalues of the matrices Q_m are the growth/decay rates corresponding to mode m. Hence the stability of mode m can be inferred from the (signs of the) eigenvalues. In Sections 3.1.2 and 3.2.2 we find the matrices Q_m and inspect their eigenvalues for two specific target configurations.

Merits and limitations of this approach. The main advantage of this approach is the dimensionality reduction. Specifically, by assuming that the perturbed states have constant densities within their supports, the problem reduces to studying stability of the perturbed boundaries – the evolution of the boundary curves depends only on the shape of the domains via integrals of the form (36) and (37). In other words, we have self-contained evolution equations for the boundaries of the perturbed domains, that allows a direct study of their stability.

The observation above brings immediate connections with similar approaches from related literature. One such approach, which concerns directly the class of aggregation models considered in his paper, applies to stability of equilibria supported on one-dimensional curves [34, 37]. Another is the interface method used to study the stability of stationary bump solutions of neural field models [27, 28, 18]. There, an interface is defined as a level set of the neural activity field; in applications, this level set is taken at the firing threshold value. It can be shown that the evolution of such an interface depends entirely on the neural field along the interface, and not on field values away from the contour. Consequently, a stand-alone equation for the evolution of the interface can be derived, and its linear stability investigated accordingly. Our approach, in identifying stable/unstable Fourier modes of the aggregations' boundaries, is very similar in spirit to the stability of neural activity interfaces in the aforementioned studies.

In terms of limitations, we restricted ourselves to circle-shaped domain boundaries primarily because we do not have an exact mathematical description for the other shapes appearing in Figure 1. Such description is required to perform the analysis of this section, starting from a modified form of (35).

Even if we did manage to find exact formulas for non-circular boundaries, it is not directly clear if we could obtain results analogous to those in Appendix B. For circular boundaries, the final result in Appendix B is based on integrals of the form (96) and (98), for which we have exact expressions. For non-circular boundaries a different parameterization in θ of $\partial\Omega_\ell^\varepsilon$ is needed in the first integral in (37). Linearization in ε of the boundary integral may again reduce the problem to the evaluation of certain basic integrals; in general, exact solutions of such integrals are not available, and numerical approximations would be needed.

Similar remarks can be made regarding our choice of potentials in (2). For generic potentials the integral (36) can be transformed into an integral of K over the boundary $\partial\Omega_\ell^\varepsilon$. Depending on the potential, one may or may not find closed expressions for these line integrals or their linearization in ε. Nevertheless, for either non-circular boundaries or generic potentials, provided no analytical progress can be made, one may still be able to make progress numerically. For instance, the matrices Q_m in (38) could be approximated using quadrature rules in each entry.

We manage to analyze the target steady states by our linear perturbation method; cf. Sections 3.1.2 and 3.2.2. These states have the advantage that there is an $\mathcal{O}(1)$ distance between the disk-shaped core and the annular region outside. Hence, for sufficiently small $\varepsilon_{j,N}$'s and $\varepsilon_{j,T}$'s, the three perturbed boundaries do not interfere.

Now consider the 'overlap' states (e.g. the one shown for $A = 0.5$ and $B = 1$ in Figure 1). The boundaries of the supports are circular, and hence (28) could in principle still be used. Examine however the boundary of the support of the lighter (red) species. For the heavier (blue) species, this *same* circle is the separating curve between the region of coexistence with the red species (central circle), and the outer annulus in which only the blue species is present. This implies that a point $x = p_j(\theta_0)$ on this inner boundary needs to satisfy *two* evolution equations: one dictated by the velocity of the blue species, and another dictated by the velocity of the red species. For the overlap state, we performed the corresponding calculations, but obtained two inconsistent equations. We did not manage to resolve this issue. It indicates however that interfering boundaries (even if they are circles) may lead to difficulties in our method.

An extra complication lies in the fact that for every boundary that appears in a certain steady state, system (38) contains two variables. Ultimately, (the signs of) the eigenvalues of the matrix Q_m in (38) need to be determined. For Q_m larger than 3×3, finding the eigenvalues analytically is in general not possible, and one needs to rely on other techniques. In this paper for

instance we inspected the coefficients of the characteristic polynomial to draw our conclusions. An alternative is to use Gershgorin's theorem (which however does not give a conclusive answer about the sign in the cases treated in this paper) or eventually numerics.

2.4 Discrete model and numerical investigation of equilibria

There is a particle system formulation that follows immediately from (1) and this system of ODE's is the basis for the numerical investigations done in this paper. We consider a total number of N particles, distributed over the two species, such that the two populations are $\{x_i^{(1)}\}_{i=1}^{N_1} \subset \mathbb{R}^2$ and $\{x_i^{(2)}\}_{i=1}^{N_2} \subset \mathbb{R}^2$, respectively, with $N_1 + N_2 = N$.

The discrete analogue of model (1) is given by the following system of ODE's:

$$\frac{dx_i^{(1)}}{dt} = -\frac{M_1}{N_1}\sum_{\substack{j=1\\ j\neq i}}^{N_1} \nabla K_s\left(x_i^{(1)} - x_j^{(1)}\right) - \frac{M_2}{N_2}\sum_{j=1}^{N_2} \nabla K_c\left(x_i^{(1)} - x_j^{(2)}\right), \quad i = 1, \dots, N_1, \tag{39a}$$

$$\frac{dx_i^{(2)}}{dt} = -\frac{M_1}{N_1}\sum_{j=1}^{N_1} \nabla K_c\left(x_i^{(2)} - x_j^{(1)}\right) - \frac{M_2}{N_2}\sum_{\substack{j=1\\ j\neq i}}^{N_2} \nabla K_s\left(x_i^{(2)} - x_j^{(2)}\right), \quad i = 1, \dots, N_2. \tag{39b}$$

Note that the four summations in the right-hand sides correspond (except for the omission of the self-interaction term) to convolutions of the interaction potentials with the empirical measures $\mu_k := 1/N_k \sum_{i=1}^{N_k} \delta_{x_i^{(k)}}$.

We investigate the steady states of the particle system numerically, by performing long-time simulations of (39) starting from random initial data. The steady states of the particle system are expected to capture the steady states of the PDE model (1). Particle simulations are in fact the main tool used to study numerically equilibria of the one species model [2, 34, 40, 26].

3 Target equilibrium

In this section we investigate the radially symmetric state where the two species are supported concentrically on a disk and an annulus, respectively. See the left-hand picture for parameter values $(A, B) = (3, 3.5)$ in Figure 1. We also consider this state with the heavy and light species interchanged. Both of them we call "targets".

3.1 Lighter species inside

Consider the target configuration sketched in Figure 4, where the heavier species 1 is supported on an annular region $R_1 < |x| < R_0$, and the lighter species 2 is supported on a disk of radius R_2, with $R_2 \leq R_1 \leq R_0$. Following simple calculations, the radii are given by

$$R_2^2 = \frac{a_s M_2}{b_c M_1 + b_s M_2}, \qquad R_1^2 = \frac{a_c M_2}{b_s M_1 + b_c M_2}, \qquad R_0^2 = \frac{a_s M_1 + a_c M_2}{b_s M_1 + b_c M_2}. \tag{40}$$

Within the respective (non-overlapping) supports $\Omega_1 = \{R_1 < |x| < R_0\}$ and $\Omega_2 = \{|x| < R_2\}$, the equilibrium densities are (cf. (10)):

$$\bar{\rho}_1 = \frac{b_s M_1 + b_c M_2}{\pi a_s}, \qquad \bar{\rho}_2 = \frac{b_c M_1 + b_s M_2}{\pi a_s}. \tag{41}$$

For consistency with the target solution ansatz, (A, B) has to lie in $D_3 \cup D_4 \cup D_5$.

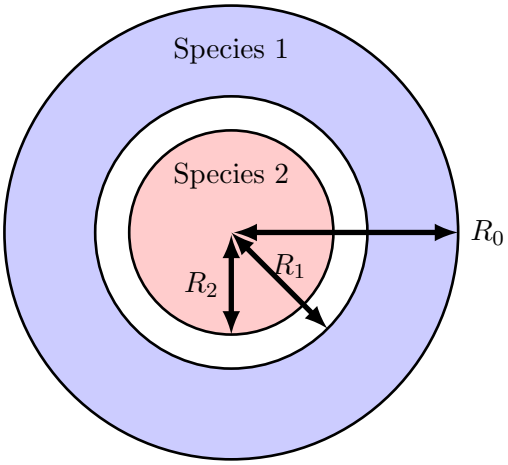

Figure 4: Target equilibrium, with species 1 supported on the annular region $R_1 < |x| < R_0$, and (the lighter) species 2 supported on a disk of radius R_2.

3.1.1 Variational approach

We now proceed to investigate whether the target equilibrium is a local minimizer with respect to class $\mathcal{B}$ perturbations, cf. (22). The following elementary calculations will be needed in the sequel:

$$\int_{|y|<R} \ln|x-y|\,\mathrm{d}y = \begin{cases} \frac{\pi}{2}|x|^2 + \pi R^2 \ln R - \frac{\pi}{2}R^2 & \text{if } |x| < R \\ \pi R^2 \ln|x| & \text{if } |x| > R, \end{cases} \tag{42}$$

and

$$\int_{|y|<R} \frac{x-y}{|x-y|^2}\,\mathrm{d}y = \begin{cases} \pi x & \text{if } |x| < R \\ \pi R^2 \frac{x}{|x|^2} & \text{if } |x| > R. \end{cases} \tag{43}$$

Note in fact that (43) can be derived from (42) by differentiation.

Calculate $\nabla\Lambda_1$ from (19a), with the potentials given by (2) and the equilibrium densities given by (41). Using (42) and (43) one can check indeed that $\nabla\Lambda_1(x) = 0$ in $R_1 < |x| < R_0$, hence $\Lambda_1(x)$ is constant in the support Ω_1 (see (21)). The calculation of $\nabla\Lambda_1(x) = \Lambda_1'(|x|)\,x/|x|$ (note the radial symmetry) outside the support Ω_1 yields the following:

$$\frac{\Lambda_1'(|x|)}{|x|} = \begin{cases} b_s M_1 + b_c M_2 - \frac{a_c}{a_s}(b_c M_1 + b_s M_2) & \text{if } |x| < R_2 \\ b_s M_1 + b_c M_2 - a_c M_2/|x|^2 & \text{if } R_2 < |x| < R_1 \\ b_s M_1 + b_c M_2 - (a_s M_1 + a_c M_2)/|x|^2 & \text{if } |x| > R_0. \end{cases} \tag{44}$$

Using the notations (3), Λ_1' in $|x| < R_2$ can be written as:

$$\Lambda_1'(|x|) = b_s M_2(M + B - A(BM+1))|x|, \qquad \text{in } |x| < R_2.$$

For all (A, B) in $D_3 \cup D_4 \cup D_5$ (see Figure 2), which is the entire parameter space where the assumed target equilibrium exists, the expression above is negative. Indeed, for such (A, B), $B > (M - A)/(MA - 1)$ (note that $MA - 1 > 0$), and hence, $ABM - B - M + A > 0$.

In $R_2 < |x| < R_1$, $\Lambda_1(|x|)$ is also decreasing, as can be seen from the simple estimate below:

$$b_s M_1 + b_c M_2 - \frac{a_c M_2}{|x|^2} < \underbrace{b_s M_1 + b_c M_2 - \frac{a_c M_2}{{R_1}^2}}_{=0 \text{ by (40)}}.$$

Finally, in $|x| > R_0$, $\Lambda_1(|x|)$ is increasing, as

$$b_s M_1 + b_c M_2 - \frac{a_s M_1 + a_c M_2}{|x|^2} > \underbrace{b_s M_1 + b_c M_2 - \frac{a_s M_1 + a_c M_2}{R_0^2}}_{=0 \text{ by (40)}}.$$

In summary, for all (A, B) in the relevant region $D_3 \cup D_4 \cup D_5$, Λ_1 satisfies (22); for an illustration see Figure 5.

We now calculate $\nabla\Lambda_2$ from (19b). By (2) and (41), also using (42) and (43) one can check indeed that $\nabla\Lambda_2(x) = 0$ in $|x| < R_2$, hence $\Lambda_2(x)$ is constant in the support Ω_2 (see (21)). The calculation of $\nabla\Lambda_2(x) = \Lambda_2'(|x|)\, x/|x|$ outside the support Ω_2 yields:

$$\frac{\Lambda_2'(|x|)}{|x|} = \begin{cases} \pi a_s \bar{\rho}_2 (1 - R_2^2/|x|^2) & \text{if } R_2 < |x| < R_1 \\ \pi a_s \bar{\rho}_2 (1 - R_2^2/|x|^2) - \pi a_c \bar{\rho}_1 (1 - R_1^2/|x|^2) & \text{if } R_1 < |x| < R_0 \\ b_c M_1 + b_s M_2 - (a_c M_1 + a_s M_2)/|x|^2 & \text{if } |x| > R_0. \end{cases} \tag{45}$$

From (45) we infer that Λ_2 is increasing in the radial direction in the region $R_2 < |x| < R_1$. On the other hand, Λ_2' can become zero in $R_1 < |x| < R_0$, and consequently Λ_2 can decrease in this region. Let us investigate this scenario. The zero of Λ_2' occurs at

$$|x|^2 = \frac{\pi a_c \bar{\rho}_1 R_1^2 - \pi a_s \bar{\rho}_2 R_2^2}{\pi a_c \bar{\rho}_1 - \pi a_s \bar{\rho}_2}. \tag{46}$$

For consistency, the expression above needs to be positive and also, it has to lie in the annular region (i.e., $R_1^2 < |x|^2 < R_0^2$). By using (41) and notations (3), the denominator in (46) reduces to:

$$\pi a_c \bar{\rho}_1 - \pi a_s \bar{\rho}_2 = M_2 b_s (M(A - B) + AB - 1).$$

Recall that the target solution only exists for parameters (A, B) in the region $D_3 \cup D_4 \cup D_5$. It is immediate to show that the expression above is negative in D_5 and positive in $D_3 \cup D_4$. Consider first the case when it is negative, i.e., $(A, B) \in D_5$. In this case, the zero of Λ_2' from (46) does not lie in the relevant region $R_1 < |x| < R_0$. In other words, for $(A, B) \in D_5$, Λ_2' does not change sign in the annular region and remains positive throughout (one can check easily for instance that $\Lambda_2'(R_1) > 0$).

For $(A, B) \in D_3 \cup D_4$, where the denominator in (46) is positive, the location of the zero given by (46) is larger than R_1 for all (A, B). By requiring that it is also less than R_0, we arrive after some elementary calculations at the following condition:

$$(M_1^2 - M_2^2)(A - B) > 0.$$

Since $M_1 > M_2$, this reduces simply to $A > B$. Hence, only for $(A, B) \in D_3$, Λ_2' can have a zero in the annular region between R_1 and R_0.

To summarize the finding above, for $(A, B) \in D_4 \cup D_5$, $\Lambda_2'(|x|)$ does not change sign and remains positive in $R_1 < |x| < R_0$. For $(A, B) \in D_3$, Λ_2 changes monotonicity in the annular region, and once it changes monotonicity, it stays decreasing through the rest of $R_1 < |x| < R_0$ – see Figure 5 for an illustration. One can check in fact that indeed, at $|x| = R_0$,

$$\Lambda_2'(R_0) = \frac{M_1^2 - M_2^2}{M_1 a_s + M_2 a_c} a_s b_s (B - A) R_0 < 0 \qquad \text{for } (A, B) \in D_3.$$

In $|x| > R_0$, it can be shown easily that Λ_2 remains strictly increasing for $(A, B) \in D_4 \cup D_5$. Consequently, combining with the findings above, the condition for Λ_2 in (22) holds for all parameter values $(A, B) \in D_4 \cup D_5$ – see Figure 5(a). For $(A, B) \in D_3$ however, it remains to be checked whether Λ_2 drops in $|x| > R_0$ below λ_2, the value it has on the support. From (45), one can infer immediately that Λ_2 changes monotonicity (again) in $|x| > R_0$, at

$$|x|^2 = \frac{a_c M_1 + a_s M_2}{b_c M_1 + b_s M_2} > R_0^2 \qquad \text{for } (A, B) \in D_3. \tag{47}$$

Denote by λ_m the value of Λ_2 at the minimum point above – see Figures 5(b) and (c). Provided $\lambda_m < \lambda_2$, then the condition for Λ_2 in (22) fails, and the target solution is not a minimizer. By

direct calculations (see Appendix A for details) we find that $\lambda_m < \lambda_2$ for parameters (A, B) that satisfy:

$$\frac{BM+1}{B+M} < \frac{AM+1}{A+M} \cdot (1+AM)^{\frac{1}{AM}} \cdot \left(1+\frac{M}{A}\right)^{-\frac{A}{M}} =: f(A). \tag{48}$$

By numerical inspection, $\frac{1}{M} < f(A) < M$, for $A > 1$, and hence (48) can be written explicitly as

$$B < \frac{Mf(A)-1}{M-f(A)}. \tag{49}$$

Figure 6 shows (shaded area) the subset of D_3 where (49) holds; for parameters (A, B) in this region, the target equilibrium is not a minimizer. For such (A, B) a typical profile of Λ_2 is illustrated in Figure 5(c). We also note that as M increases to infinity, the subset seems to approach the entire domain D_3.

For (A, B) in D_3 outside the shaded region, (49) is violated and hence, $\lambda_m > \lambda_2$ and (22) holds; a typical profile of Λ_2 in this case is shown in Figure 5(b).

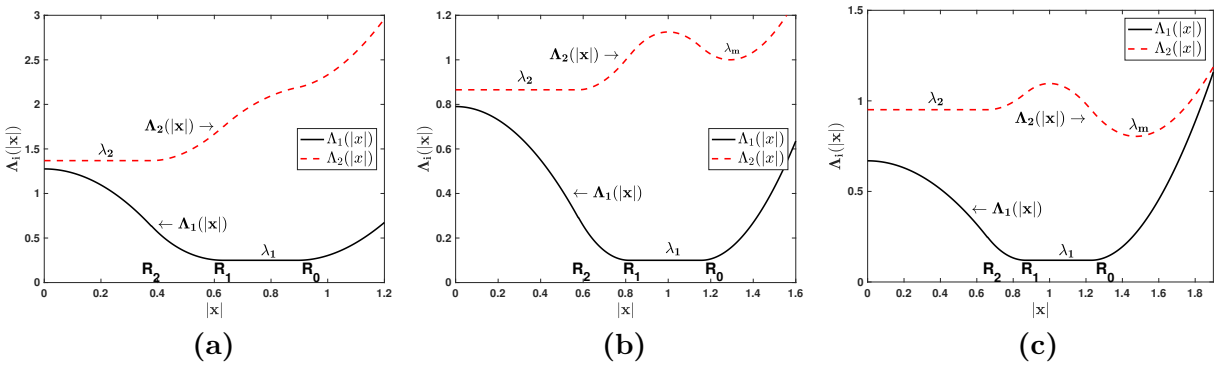

Figure 5: Typical profiles of Λ_1 and Λ_2 corresponding to the target with lighter species inside. The profiles have been shifted vertically for a better visualization. (a) (A, B) in $D_4 \cup D_5$, (b) (A, B) in the subset of D_3 where (22) holds ($\lambda_m > \lambda_2$), (c) (A, B) in D_3 where (22) fails ($\lambda_m < \lambda_2$) – see also shaded areas in Figure 6. In (a) and (b) the target is a local minimizer with respect to perturbations of class $\mathcal{B}$. The equilibrium is not a minimizer in (c) – see also Remark 3.1.

Remark 3.1. *With regard to Figure 5(c), we note that $\Lambda_2(x) \geq \lambda_2$ (see (22)) is satisfied for x in a neighbourhood of Ω_2 (i.e., for $|x|$ near R_2). Consequently, such an equilibrium is a minimizer with respect to redistributions of mass within a (certain) neighbourhood of the equilibrium's support; such equilibria are referred in [5] as swarm minimizers. For this reason, in the formal variational approach from [2] this equilibrium would be a local minimizer in the ∞-Wasserstein topology, but not in the 2-Wasserstein topology.*

To conclude, we have derived:

Proposition 3.2 (Local minimum)**.** *The target equilibrium in Figure 4 is a local minimizer in $\mathcal{F}$ with respect to perturbations of class $\mathcal{B}$ for all values of (A, B) in D_4 and D_5. Moreover, it is also a local minimizer with respect to such perturbations in the subset of D_3 where (49) is false (unshaded areas in Figure 6).*

We note that for general parameter values (A, B) we have not investigated perturbations of class $\mathcal{A}$ because of the difficulties pointed out in Section 2.2. Nevertheless, by the considerations made in Section 2.2, the second variation of the energy is positive for *both* classes of perturbations when $a_s > a_c$ and $b_c > b_s$ (or equivalently, $A < 1$ and $B > 1$) – see (23), (25) and (26)). Also recall that the considerations there were made for compactly supported perturbations (minimization in $\mathcal{F}_c \subset \mathcal{F}$). From this observation we infer:

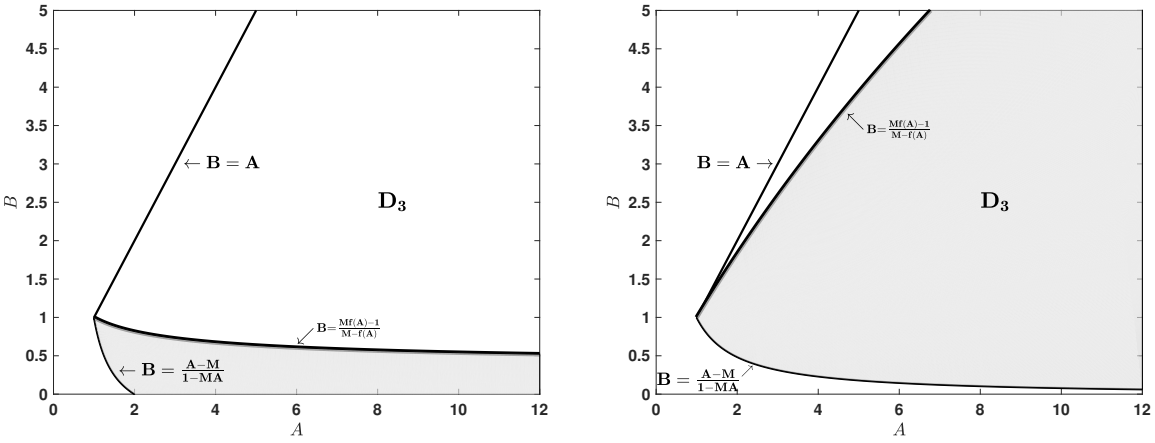

(a) **(b)**

Figure 6: Shaded areas represent the subsets of D_3 where (49) holds, for (a) $M = 2$ and (b) $M = 50$. For parameters in this region, the target equilibrium with the lighter species inside is not a local minimizer with respect to perturbations of class $\mathcal{B}$. Note that the regions where the target is not a minimizer tends to cover the entire D_3 as $M \to \infty$.

Theorem 3.3 (Global minimum)**.** *The target equilibrium in Figure 4 is a* global *minimizer in $\mathcal{F}_c$ (with respect to both class $\mathcal{A}$ and class $\mathcal{B}$ perturbations) for all (A, B) in D_5 with $A < 1$ (note that $B > 1$ in D_5); i.e. in the intersection of D_5 with the shaded region in Figure 2.*

Despite being derived by unsophisticated, elementary methods, Theorem 3.3 is a very strong result that illustrates the high relevance of this target equilibrium. Regarding Proposition 3.2, our numerical investigations of the particle system (39) suggest that the target equilibrium is *only* stable in $D_4 \cup D_5$. Some indication that this state is unstable in D_3 is given by the fact that the region (49) where the target is not a minimizer tends to cover the whole of D_3 as $M \to \infty$. Although we do not have the tools to show it, we conjecture that this state is a local minimizer with respect to perturbations of class $\mathcal{A}$ in $D_4 \cup D_5$, but not in D_3. It turns out that linear stability analysis supports this claim, as shown in the next section.

3.1.2 Linear stability analysis

In this section we derive the following result:

Theorem 3.4 (Linear stability)**.** *The target configuration in Figure 4 is a linearly stable steady state only for $(A, B) \in D_4 \cup D_5$.*

We first have to obtain the evolution equations on the boundaries for this specific configuration. We apply perturbations (28) to each of the three boundaries and follow the lines of Section 2.3 to arrive at a linearized system (38). To that aim, we have to find (linearized) expressions for the right-hand sides in

$$\frac{d}{dt}p_0(\theta_0, t) = v_1(p_0(\theta_0, t)), \quad \frac{d}{dt}p_1(\theta_0, t) = v_1(p_1(\theta_0, t)), \quad \text{and} \quad \frac{d}{dt}p_2(\theta_0, t) = v_2(p_2(\theta_0, t)). \tag{50}$$

These right-hand sides involve integrals of the forms (36) and (37). For the outer (perturbed) annulus we have the difference of two such integrals, since the support of species 1 is $\Omega_0^\varepsilon(t) \setminus \Omega_1^\varepsilon(t)$.

For instance, we have that

$$\frac{d}{dt}p_0(\theta_0,t) = a_s\,\bar\rho_1 \int\limits_{\Omega_0^\varepsilon(t)} \frac{x-y}{|x-y|^2}\,dy - b_s\,\bar\rho_1 \int\limits_{\Omega_0^\varepsilon(t)} (x-y)\,dy$$
$$- \left(a_s\,\bar\rho_1 \int\limits_{\Omega_1^\varepsilon(t)} \frac{x-y}{|x-y|^2}\,dy - b_s\,\bar\rho_1 \int\limits_{\Omega_1^\varepsilon(t)} (x-y)\,dy \right) + a_c\,\bar\rho_2 \int\limits_{\Omega_2^\varepsilon(t)} \frac{x-y}{|x-y|^2}\,dy - b_c\,\bar\rho_2 \int\limits_{\Omega_2^\varepsilon(t)} (x-y)\,dy,$$

with $x = p_0(\theta_0,t)$. Expressions (up to higher-order terms) of the appearing integrals are given in Appendix B. We use (30) for the left-hand sides, divide each linearized equation in (50) by $R_j \exp(i\,\theta_0)$ and match sine and cosine terms on both sides of the equation. The result is six equations that are independent of the choice of θ_0. Together, for each $m \in \mathbb{N}^+$ these form a system (38), where we denote $\underline{\varepsilon} := (\varepsilon_{0,N}, \varepsilon_{0,T}, \varepsilon_{1,N}, \varepsilon_{1,T}, \varepsilon_{2,N}, \varepsilon_{2,T})^T$.

As anticipated in Section 2.3, we indeed verified using (40) and (41) that the $\mathcal{O}(1)$ terms have zero contribution; this is a necessary condition for the target $\underline{\varepsilon} = 0$ to be a steady state.

The matrix Q_m is given by

$$Q_1 := \begin{bmatrix}
-a_s\,\pi\,\bar\rho_1 + b_s\bar\rho_1\pi R_0^2 & 0 & -a_s\bar\rho_1\pi\left(\frac{R_1}{R_0}\right)^3 - b_s\bar\rho_1\pi\frac{R_1^3}{R_0} & 0 & \frac{M_2 a_c R_2}{R_0^3} + \frac{M_2 b_c R_2}{R_0} & 0 \\
a_s\,\pi\,\bar\rho_1 - b_s\,\bar\rho_1\,\pi\,R_0^2 & 0 & -a_s\,\pi\,\bar\rho_1\left(\frac{R_1}{R_0}\right)^3 + b_s\,\bar\rho_1\,\pi\,\frac{R_1^3}{R_0} & 0 & \frac{M_2\,a_c\,R_2}{R_0^3} - \frac{M_2\,b_c\,R_2}{R_0} & 0 \\
-a_s\pi\bar\rho_1\frac{R_0}{R_1} + b_s\bar\rho_1\pi\frac{R_0^3}{R_1} & 0 & -a_s\,\pi\,\bar\rho_1 - b_s\bar\rho_1\pi R_1^2 & 0 & \frac{M_2 a_c R_2}{R_1^3} + \frac{b_c M_2 R_2}{R_1} & 0 \\
a_s\pi\bar\rho_1\frac{R_0}{R_1} - b_s\bar\rho_1\pi\frac{R_0^3}{R_1} & 0 & -a_s\pi\bar\rho_1 + b_s\pi\bar\rho_1 R_1^2 & 0 & \frac{M_2 a_c R_2}{R_1^3} - \frac{M_2 b_c R_2}{R_1} & 0 \\
-a_c\pi\bar\rho_1\frac{R_0}{R_2} + b_c\pi\bar\rho_1\frac{R_0^3}{R_2} & 0 & a_c\pi\bar\rho_1\frac{R_1}{R_2} - b_c\bar\rho_1\pi\frac{R_1^3}{R_2} & 0 & -M_1\,b_c & 0 \\
a_c\pi\bar\rho_1\frac{R_0}{R_2} - b_c\bar\rho_1\pi\frac{R_0^3}{R_2} & 0 & -a_c\pi\bar\rho_1\frac{R_1}{R_2} + b_c\bar\rho_1\pi\frac{R_1^3}{R_2} & 0 & M_1\,b_c & 0
\end{bmatrix} \tag{51}$$

for mode $m = 1$, and for any other mode $m \geqslant 2$ by

$$Q_m := \begin{bmatrix}
-a_s\,\pi\,\bar\rho_1 & 0 & -a_s\,\pi\,\bar\rho_1\left(\frac{R_1}{R_0}\right)^{m+2} & 0 & a_c\,\pi\,\bar\rho_2\left(\frac{R_2}{R_0}\right)^{m+2} & 0 \\
a_s\,\pi\,\bar\rho_1 & 0 & -a_s\,\pi\,\bar\rho_1\left(\frac{R_1}{R_0}\right)^{m+2} & 0 & a_c\,\pi\,\bar\rho_2\left(\frac{R_2}{R_0}\right)^{m+2} & 0 \\
-a_s\pi\bar\rho_1\left(\frac{R_1}{R_0}\right)^{m-2} & 0 & -a_s\,\pi\bar\rho_1 & 0 & a_c\,\pi\,\bar\rho_2\left(\frac{R_2}{R_1}\right)^{m+2} & 0 \\
a_s\pi\bar\rho_1\left(\frac{R_1}{R_0}\right)^{m-2} & 0 & -a_s\pi\bar\rho_1 & 0 & a_c\,\pi\,\bar\rho_2\left(\frac{R_2}{R_1}\right)^{m+2} & 0 \\
-a_c\pi\bar\rho_1\left(\frac{R_2}{R_0}\right)^{m-2} & 0 & a_c\pi\bar\rho_1\left(\frac{R_2}{R_1}\right)^{m-2} & 0 & -a_s\pi\bar\rho_2 & 0 \\
a_c\pi\bar\rho_1\left(\frac{R_2}{R_0}\right)^{m-2} & 0 & -a_c\pi\bar\rho_1\left(\frac{R_2}{R_1}\right)^{m-2} & 0 & a_s\pi\bar\rho_2 & 0
\end{bmatrix}. \tag{52}$$

The signs of the eigenvalues of Q_m determine the stability of mode $m \geqslant 1$. The essence of the matrices Q_m is represented by 3×3 matrices consisting of only those entries of Q_m that appear in odd rows and odd columns. This is closely related to what happens when one computes $\det(Q_m - \lambda\,I)$ by a cofactor expansion with respect to the second, fourth and sixth row.

For mode $m = 1$, the characteristic polynomial only has terms of order 4 and higher. Hence, four eigenvalues are zero. The remaining two eigenvalues can be found explicitly using the quadratic formula. They are real and one of them is always negative. The other one is negative if and only if $B > A$. Recall that this target equilibrium only exists in $D_3 \cup D_4 \cup D_5$. Consequently, mode $m = 1$ is unstable in the region D_3, and stable in $D_4 \cup D_5$.

The eigenvectors corresponding to zero eigenvalues are

$$(0,1,0,0,0,0)^T, \qquad (0,0,0,1,0,0)^T, \qquad (0,0,0,0,0,1)^T, \quad \text{and}$$
$$\left(\frac{1}{R_0}, -\frac{1}{R_0}, \frac{1}{R_1}, -\frac{1}{R_1}, \frac{1}{R_2}, -\frac{1}{R_2}\right)^T.$$

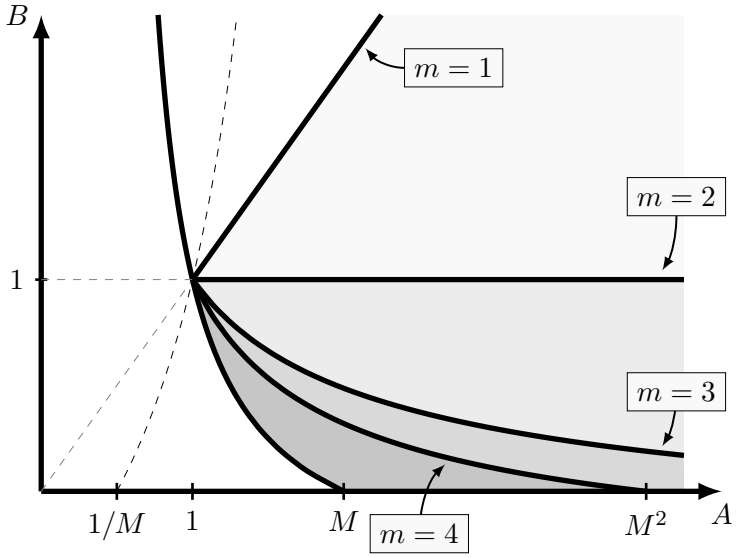

Figure 7: The boundaries of the regions U_m for $m = 1, 2, 3, 4$. Note that $U_4 \subset U_3 \subset U_2 \subset U_1$.

The first three correspond to tangential perturbations of a single one of the boundaries which –to leading order– does not change its shape. The latter eigenvector corresponds to translation of all three boundaries simultaneously over the same distance. Such translations constitute a translation of the total centre of mass, under which the system is invariant; see (6). A prefactor R_j is present in (35), hence each component of the eigenvector contains an appropriate factor $1/R_j$ so that each boundary is translated over the same j-independent distance.

To further asses the stability in $D_4 \cup D_5$, we are required to investigate the eigenvalues for all higher-order modes. For general $m \geqslant 2$ the characteristic polynomial only has terms of order three and higher. Hence there are three eigenvalues zero, corresponding to tangential perturbations of one of the boundaries.

Given the fact that there are three eigenvalues zero, it is immediate to find the third-order polynomial P of which the remaining eigenvalues are roots. Call these roots *nontrivial eigenvalues*. Careful inspection of the sign of the constant term of P, yields that there is at least one (real and) positive eigenvalue if $(A, B) \in U_m$, with

$$U_m := \left\{ (A,B) \in D_3 \cup D_4 \cup D_5 \ : \ 1 < A < M^{\frac{m}{m-2}} \text{ and } 0 < B < \frac{MA^{\frac{2}{m}} - A}{MA - A^{\frac{2}{m}}} \right\}.$$

Here, it is understood that $M^{\frac{m}{m-2}} = \infty$ for $m = 2$, and U_2 is $\{1 < A < \infty, 0 < B < 1\} \cap (D_3 \cup D_4 \cup D_5)$. Define $U_1 := D_3$, the region where mode $m = 1$ is unstable. For $n > m \geqslant 1$ it holds that $U_n \subset U_m$. See Figure 7 for an indication of the boundaries of the regions U_m and the way in which U_{m+1} is contained in U_m.

Let S_m be the complement of U_m in $D_3 \cup D_4 \cup D_5$ (excluding the boundary). For $(A, B) \in S_m$, if we evaluate the polynomial P at appropriate negative values, we can identify three sign changes, hence P has three real and negative roots. Consequently, all (nontrivial) eigenvalues of Q_m are real and negative in S_m for any $m \geqslant 2$. Thus mode $m \geqslant 2$ is stable in S_m and moreover we have that $S_m \subset S_n$ if $n > m \geqslant 1$. We showed before that mode $m = 1$ is stable if and only if $(A, B) \in D_4 \cup D_5 =: S_1$. Hence we have showed the stability of the target (lighter species inside) for all modes $m \geqslant 1$ provided that $(A, B) \in S_1 = D_4 \cup D_5$.

3.2 Heavier species inside

In this equilibrium state the (heavier) species 1 is supported in the disk $|x| < R_1$, and the (lighter) species 2 is supported on the annulus $R_2 < |x| < R_0$, with $R_1 \leq R_2 \leq R_0$ – see Figure

8.

Calculations lead to

$$R_1^2 = \frac{a_s M_1}{b_s M_1 + b_c M_2}, \qquad R_2^2 = \frac{a_c M_1}{b_c M_1 + b_s M_2}, \qquad R_0^2 = \frac{a_c M_1 + a_s M_2}{b_c M_1 + b_s M_2}. \tag{53}$$

The equilibrium densities are given by (41) (cf. (10)). For consistency with the solution ansatz, (A, B) has to lie in $D_2 \cup D_3 \cup D_4$.

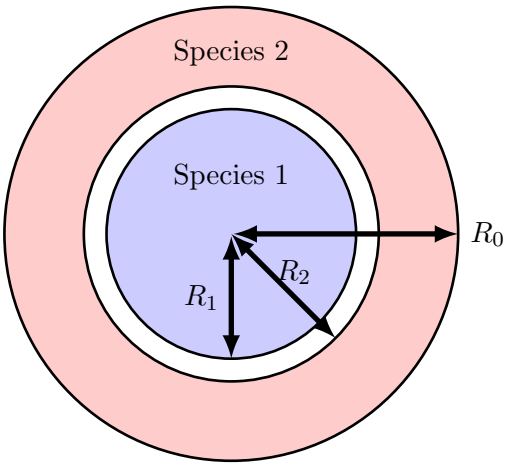

Figure 8: Target equilibrium, with species 1 supported on a disk of radius R_1, and (the lighter) species 2 supported on the annular region $R_2 < |x| < R_0$.

3.2.1 Variational approach

The calculations of Λ_1' and Λ_2' mirror the ones in Section 3.1.1. The results are:

$$\frac{\Lambda_1'(|x|)}{|x|} = \begin{cases} \pi a_s \bar{\rho}_1 (1 - R_1^2/|x|^2) & \text{if } R_1 < |x| < R_2 \\ \pi a_s \bar{\rho}_1 (1 - R_1^2/|x|^2) - \pi a_c \bar{\rho}_2 (1 - R_2^2/|x|^2) & \text{if } R_2 < |x| < R_0 \\ b_s M_1 + b_c M_2 - (a_s M_1 + a_c M_2)/|x|^2 & \text{if } |x| > R_0, \end{cases} \tag{54}$$

and

$$\frac{\Lambda_2'(|x|)}{|x|} = \begin{cases} b_c M_1 + b_s M_2 - \frac{a_c}{a_s}(b_s M_1 + b_c M_2) & \text{if } |x| < R_1 \\ b_c M_1 + b_s M_2 - a_c M_1/|x|^2 & \text{if } R_1 < |x| < R_2 \\ b_c M_1 + b_s M_2 - (a_c M_1 + a_s M_2)/|x|^2 & \text{if } |x| > R_0. \end{cases} \tag{55}$$

Also note that Λ_1' and Λ_2' vanish on the respective supports of $\bar{\rho}_1$ and $\bar{\rho}_2$: $\{|x| < R_1\}$ and $\{R_2 < |x| < R_0\}$; cf. (21).

It is immediate to check that Λ_2 (corresponding to the lighter species) for all (A, B) in the relevant region $D_2 \cup D_3 \cup D_4$ satisfies (22).

As in Section 3.1.1, the calculations for the heavier species are slightly more involved and do not always lead to the minimization condition (22). From (54), one concludes easily that $\Lambda_1'(|x|) > 0$ in $R_1 < |x| < R_2$. However, Λ_1' can become zero in $R_2 < |x| < R_0$, and hence Λ_1 can decrease in this region. The zero of Λ_1' occurs at

$$|x|^2 = \frac{\pi a_s \bar{\rho}_1 R_1^2 - \pi a_c \bar{\rho}_2 R_2^2}{\pi a_s \bar{\rho}_1 - \pi a_c \bar{\rho}_2} = \frac{M_1 a_s (1 - A^2)}{M_2 b_s (M + B - A(BM + 1))}, \tag{56}$$

The denominator of (56) is positive in D_2 and negative in $D_3 \cup D_4$. Consider first the case when it is positive, i.e., $(A, B) \in D_2$. Since the denominator is positive, the numerator has to be positive as well (i.e., $A < 1$). It is then a simple exercise to show that the zero of Λ_1' from

(56) does not lie in the relevant region $R_2 < |x| < R_0$. Hence, for $(A, B) \in D_2$, Λ_1' does not change sign in the annular region and remains positive throughout (as a check we found indeed that $\Lambda_1'(R_0) > 0$).

For $(A, B) \in D_3 \cup D_4$, where the denominator in (56) is negative, the numerator is also negative (as $A > 1$ there). Also, the location of the zero given by (56) is larger than R_2 for all $(A, B) \in D_3 \cup D_4$. We require that it is also less than R_0 and we arrive after some elementary calculations to the following condition:

$$(M_1^2 - M_2^2)(A - B) < 0.$$

Since $M_1 > M_2$, to have a zero of Λ_1' in the annular region one needs $A < B$, i.e., $(A, B) \in D_4$. Otherwise, for $(A, B) \in D_3$, Λ_1' does not change sign and remains positive in the annular region.

Finally, in $|x| > R_0$, it can be shown that Λ_1 remains strictly increasing for $(A, B) \in D_2 \cup D_3$, where $A > B$. Combined with the findings above (including the calculations for Λ_2), we infer that (22) holds for all parameter values $(A, B) \in D_2 \cup D_3$.

On the other hand, for $(A, B) \in D_4$, Λ_1 changes monotonicity in $|x| > R_0$, at

$$|x|^2 = \frac{a_s M_1 + a_c M_2}{b_s M_1 + b_c M_2} > R_0^2 \qquad \text{for } (A, B) \in D_4. \tag{57}$$

If Λ_1 evaluated at the minimum point above drops below λ_1, then the condition for Λ_1 in (22) fails, and this target solution is not a minimizer. We do not present these calculations, we only list the end result. Following calculations similar to the other target equilibrium (see (48)), we find that the target with the heavier species inside is *not* a local minimizer provided

$$\frac{B + M}{BM + 1} < \frac{A + M}{AM + 1} \cdot \left(1 + \frac{A}{M}\right)^{\frac{M}{A}} \cdot \left(1 + \frac{1}{AM}\right)^{-AM}. \tag{58}$$

The inequality (58), which can be rearranged to be explicit in B, describes a subset of D_4 which grows with the mass ratio M. For the rest of $(A, B) \in D_4$, $\lambda_m > \lambda_1$ and hence (22) holds. Thus, we have derived:

Proposition 3.5. *The target equilibrium with the heavier species inside is a local minimizer in $\mathcal{F}$ with respect to class $\mathcal{B}$ perturbations for all $(A, B) \in D_2 \cup D_3$ and for $(A, B) \in D_4$ for which* (58) *is violated.*

In our numerical investigations of the particle system (39) we never observed the target equilibrium from Figure 8 as a numerical steady state, and hence we conjecture that it is not stable. In particular, given Proposition 3.5 we conjecture that this state is unstable with respect to class $\mathcal{A}$ perturbations in D_2, D_3 and (the indicated part of) D_4, although we do not have the means to prove this. But, as we show in the next section, the linear stability analysis is in agreement with this claim.

3.2.2 Linear stability analysis

In this section we demonstrate the following result:

Theorem 3.6 (Linear instability)**.** *The target configuration in Figure 8 is linearly unstable for any set of parameters (A, B) for which this equilibrium exists, i.e., for any $(A, B) \in D_2 \cup D_3 \cup D_4$.*

For this steady state, we can obtain the corresponding matrices Q_m (for $m \geqslant 1$) in (38) directly from (51) and (52) by writing those matrices fully in terms of a_s, a_c, b_s, b_c, M_1 and M_2 and subsequently interchanging M_1 and M_2. These matrices correspond to the system of ODE's (38) where in fact $\underline{\varepsilon} := (\varepsilon_{0,N}, \varepsilon_{0,T}, \varepsilon_{2,N}, \varepsilon_{2,T}, \varepsilon_{1,N}, \varepsilon_{1,T})^T$ is reordered, in agreement with the ordering of R_0, R_2 and R_1 in Figure 8. Alternatively, we could have derived these matrices starting from the building blocks in Appendix B, analogously to what we did in Section 3.1.2.

The characteristic polynomial of Q_1 has only terms of order four and higher. Hence, there are four eigenvalues zero; cf. Section 3.1.2. The other two eigenvalues can be calculated explicitly, and these are real. One of them is always negative and the other one is negative if and only if $B > A$; i.e. for $(A, B) \in D_4$. Hence, this state is unstable in $D_2 \cup D_3$ where one eigenvalue is positive.

For mode $m = 2$, we find that the characteristic polynomial has terms only of order three and higher. There are three eigenvalues zero, and the other three *nontrivial* eigenvalues are roots of some polynomial $\tilde{P}$ (which we can find explicitly). The constant term of this polynomial equals the product of the three nontrivial eigenvalues, and we observe that there is at least one positive eigenvalue if this constant is positive. This argument holds when all eigenvalues are real and also when two eigenvalues are complex conjugates. Here, it is thus not even necessary to verify whether the roots of the characteristic polynomial are real. One can check that the product of the nontrivial eigenvalues is positive if $B > 1$. Consequently, mode $m = 2$ is unstable if $B > 1$.

We previously concluded that mode $m = 1$ is unstable in $D_2 \cup D_3$. It follows that modes 1 and 2 are never stable simultaneously, and hence this target steady state must be unstable for any choice of $(A, B) \in D_2 \cup D_3 \cup D_4$.

3.3 Numerical illustration of the unstable modes

3.3.1 Target: lighter species inside

In Section 3.1 we derived that the target state (with the lighter species inside) is stable in $D_4 \cup D_5$. Mode 1 is unstable in region D_3, while mode 2 is unstable for $B < 1$. The instability regions for the higher-order modes are such that for mode m this region is a subset of the instability region for mode $m - 1$. See Section 3.1.2 for the full details.

Here, we further illustrate the instability. First we run a particle system of 200 particles with $M = 2$ and $(A, B) = (3, 3.5)$. The system approaches the target steady state shown in Figure 1 at the top. Next we choose two pairs of parameter values such that $1 < B < A$, and $B < 1$, respectively. Specifically, we take $(A, B) = (3, 2)$ and $(A, B) = (3, 0.75)$. For the latter parameter pair, mode 2 is unstable, but mode 3 and higher are still stable.

We start from the target particle configuration that follows from the numerics for $(3, 3.5)$. To obtain the correct target ansatz for our new choice of parameters (A, B), we subsequently rescale this configuration using (40). We then perform a numerical run of (39), both for $(A, B) = (3, 2)$ and for $(A, B) = (3, 0.75)$. Some snapshots are shown in Figure 9. As expected, for $(A, B) = (3, 2)$ a mode 1 instability occurs (this is the only unstable mode), shifting the red core outside. For $(A, B) = (3, 0.75)$, when modes 1 and 2 are both unstable, we again observe a mode 1 instability. Apparently, mode 1 dominates mode 2 here (larger eigenvalue in the linearized system of Section 3.1.2).

3.3.2 Target: heavy species inside

In Section 3.2 we focussed on the target state when the heavy species is inside the light species. We showed that is unstable. Hence we do not observe it numerically. In particular, mode 1 is unstable in region $D_2 \cup D_3$; that is, for $B < A$. We also showed that mode 2 is unstable if $B > 1$. See Section 3.2.2.

These different modes of instability will be illustrated here. We again design a particle system of 200 particles with $M = 2$ and now we pick three pairs of parameter values such that first $B > A$, next $1 < B < A$, and finally $B < 1$. We construct a target configuration with the heavy species inside and with radii according to (53) to resemble the target ansatz. Since the target with the heavy species inside is unstable, it does not appear as a steady state in numerical simulations. Therefore, some manipulation is needed to obtain the target that we use as initial configurations. We omit further details.

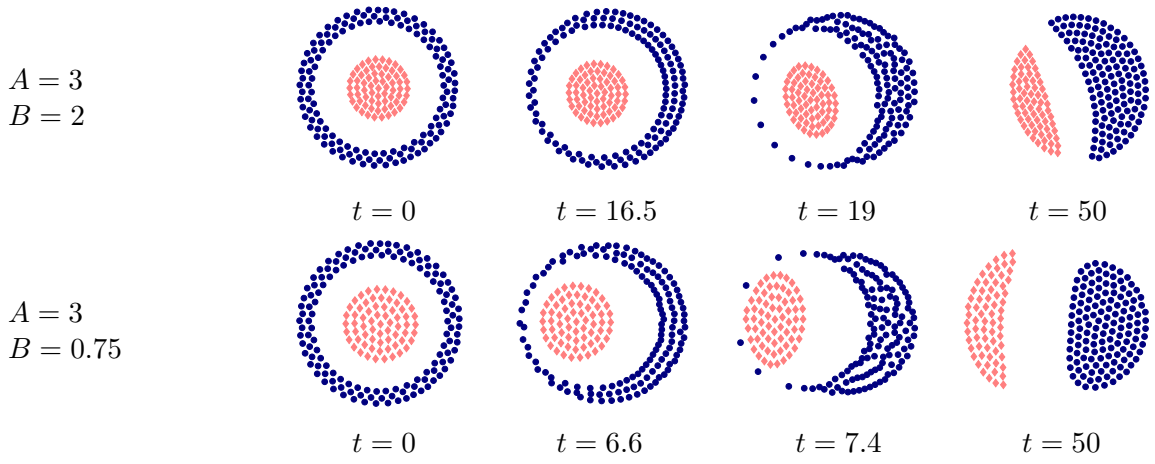

Figure 9: Steady states that arise, starting from the target configuration with the lighter species inside. Apparently, for $B < A$, the mode 1 instability is dominant in the transition into a non-radially symmetric steady state. This is even the case when mode 2 is also unstable (see the plots for $B = 0.75$).

In Figure 10 we show snapshots of the time evolution for $(A, B) = (3, 3.5)$, and $(A, B) = (3, 2)$, and $(A, B) = (3, 0.75)$. In each case we start from the (properly scaled) target with the heavy species inside.

For $(A, B) = (3, 3.5)$, mode 2 is unstable, while mode 1 is stable. In the top row of Figure 10 we clearly see the mode 2 instability that elongates the blue core and triggers the system to evolve into a non-radially symmetric state. For $(A, B) = (3, 2)$ both modes 1 and 2 are unstable. The middle row of Figure 10 shows that apparently the mode 2 instability is dominant. The steady state that follows resembles the one in the top row. Mode 2 is stable for $(A, B) = (3, 0.75)$, but mode 1 is not. In the bottom row of Figure 10 the instability of mode 1 is visible as a translation of the blue core.

Note that the steady state on the bottom row of Figure 10 is the same as the steady state at the bottom of Figure 9. However, the former arises due to a translation (mode 1 instability) of the blue core (species 1), while the latter arises due to a mode 1 instability of the red core (species 2).

The steady states obtained in Figures 9 and 10 were previously illustrated in Figure 1.

4 Overlap equilibrium

In this section we investigate the radially symmetric state where the two species are supported on concentric disks and thus there is a region in which the two species coexist (overlap) – see the picture for parameter values $(A, B) = (0.5, 1)$ in Figure 1. We also consider two versions of this state: one where the coexistence region is surrounded by a ring of the heavier species (i.e. lighter species inside), and one with the heavy and light species interchanged (heavier species inside).

For overlap equilibria we were not able to develop a linear stability analysis as for the target solution (Sections 3.1.2 and 3.2.2). The difficulties are the ones pointed out in Section 2.3: at the boundary at R_2 the velocities of both species 1 and species 2 need to be taken into consideration. That is,

$$\frac{d}{dt}p_2(\theta_0, t) = v_1(p_2(\theta_0, t)) \qquad \text{and} \qquad \frac{d}{dt}p_2(\theta_0, t) = v_2(p_2(\theta_0, t))$$

should be satisfied. These two equations simultaneously lead to inconsistencies in our approach. For this reason the considerations in this sections are limited to the variational approach.

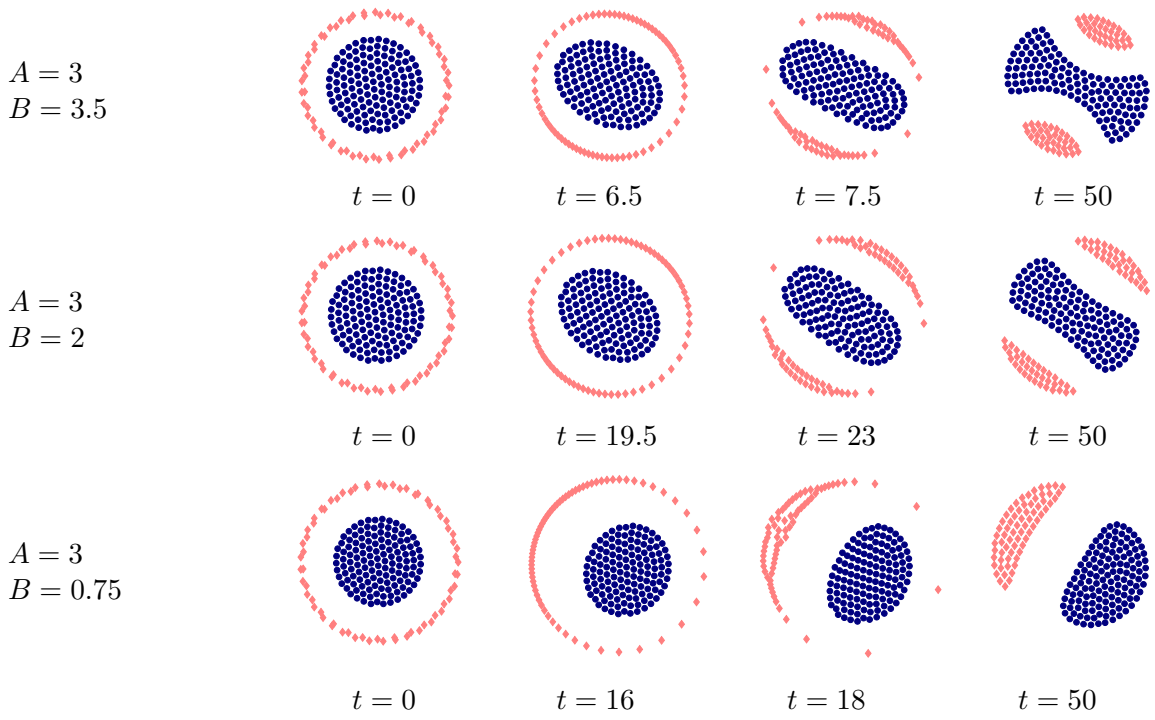

Figure 10: Steady states that arise, starting from the target configuration with the heavy species inside. For $B > 1$, mode 2 is either unstable while mode 1 is not (for $B > A$, see the plots for $B = 3.5$), or it apparently dominates mode 1, that is also unstable (for $1 < B < A$, see the plots for $B = 2$). For $B < 1$, mode 1 is unstable, while mode 2 is stable (see the plots for $B = 0.75$). Apparently the instability is driven by modes 1 or 2, and not by the higher-order modes.

4.1 Lighter species inside

In this equilibrium state species 1 and 2 are supported in disks of radii R_1 and R_2, respectively, with $R_2 < R_1$ – see Figure 11. Within $|x| < R_2$, where the two species coexist, the equilibrium densities are (see (10)):

$$\bar\rho_1 = \frac{(a_s b_s - a_c b_c)M_1 + (a_s b_c - a_c b_s)M_2}{\pi(a_s^2 - a_c^2)}, \qquad \bar\rho_2 = \frac{(a_s b_c - a_c b_s)M_1 + (a_s b_s - a_c b_c)M_2}{\pi(a_s^2 - a_c^2)}. \tag{59}$$

In the annular region $R_2 < |x| < R_1$, only species 1 is present, with equilibrium density (also see (10)):

$$\rho_1^{\text{out}} = \frac{b_s M_1 + b_c M_2}{\pi a_s}. \tag{60}$$

By immediate calculations, the radii of the two disks are found to be

$$R_1^2 = \frac{a_s M_1 + a_c M_2}{b_s M_1 + b_c M_2}, \qquad R_2^2 = \frac{(a_s^2 - a_c^2)M_2}{(a_s b_c - a_c b_s)M_1 + (a_s b_s - a_c b_c)M_2}. \tag{61}$$

Together with the consistency condition $R_2 < R_1$, it can be shown that the overlap equilibrium above exists for $(A, B) \in D_3 \cup D_6$. Note that $A > B$ in D_3, while in D_6 one has $A < B$.

Calculate $\nabla\Lambda_1$ from (19a), with equilibrium densities given by (59) and (60). Using (43) one can check indeed that $\nabla\Lambda_1(x) = 0$ in $|x| < R_2$ and $R_2 < |x| < R_1$, hence $\Lambda_1(x)$ is constant in the support of $\bar\rho_1$ (see (21)). Outside the support, in $|x| > R_1$, one finds

$$\Lambda_1'(|x|) = \big((b_s M_1 + b_c M_2)|x|^2 - (a_s M_1 + a_c M_2)\big)/|x|. \tag{62}$$

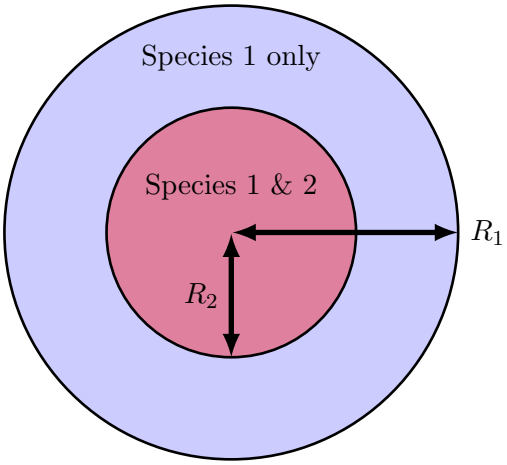

Figure 11: Overlap equilibrium, with species 1 and 2 coexisting on a disk of radius R_2, and (the heavier) species 1 also being present in the annular region $R_2 < |x| < R_1$.

From (62) and the expression of R_1 in (61), we conclude that Λ_1 is radially increasing in $|x| > R_1$, and hence, for all (A, B) in the relevant region $D_3 \cup D_6$, Λ_1 satisfies (22).

We now calculate $\nabla\Lambda_2$ from (19b). First, one can check that $\nabla\Lambda_2(x) = 0$ in $|x| < R_2$, hence $\Lambda_2(x)$ is constant in the support of $\bar{\rho}_2$; cf. (21). Then, the calculation of $\nabla\Lambda_2(x) = \Lambda_2'(|x|)\, x/|x|$ outside the support yields:

$$\frac{\Lambda_2'(|x|)}{|x|} = \begin{cases} b_c M_1 + b_s M_2 - (a_c M_1 + a_s M_2)/|x|^2 - \pi a_c \rho_1^{\text{out}}(1 - R_1^2/|x|^2) & \text{if } R_2 < |x| < R_1 \\ b_c M_1 + b_s M_2 - (a_c M_1 + a_s M_2)/|x|^2 & \text{if } |x| > R_1. \end{cases} \tag{63}$$

Consider case $(A, B) \in D_6$ first. By (61), in $|x| > R_1$ we have

$$\begin{aligned} b_c M_1 + b_s M_2 - (a_c M_1 + a_s M_2)/|x|^2 &> b_c M_1 + b_s M_2 - (a_c M_1 + a_s M_2)\frac{b_s M_1 + b_c M_2}{a_s M_1 + a_c M_2} \\ &= b_s M_2 \left(BM + 1 - (AM + 1)\frac{M + B}{M + A} \right) \\ &= b_s M_2 \frac{(B - A)(M^2 - 1)}{M + A} \end{aligned}$$

As $B > A$ for $(A, B) \in D_6$ and $M > 1$, the expression above is positive, and consequently, $\Lambda_2(x)$ is radially increasing in $|x| > R_1$.

In $R_2 < |x| < R_1$, by (60) and (3), the expression on the right-hand-side of (63) can be rewritten as:

$$b_c M_1 + b_s M_2 - (b_s M_1 + b_c M_2)A + \underbrace{\big((a_s M_1 + a_c M_2)A - a_c M_1 - a_s M_2\big)}_{= a_s M_2 (A^2 - 1) < 0 \text{ in } D_6} / |x|^2, \tag{64}$$

and hence, also using (61),

$$\frac{\Lambda_2'(|x|)}{|x|} > b_c M_1 + b_s M_2 - (b_s M_1 + b_c M_2)A + a_s M_2 (A^2 - 1)/R_2^2 \; = \; 0.$$

We conclude that Λ_2 is radially increasing in $|x| > R_2$. Since Λ_1 and Λ_2 satisfy (22), the overlap solution is a local minimizer (with respect to perturbations of class $\mathcal{B}$) when $(A, B) \in D_6$.

Next, consider the case $(A, B) \in D_3$, and take the expression for the right-hand-side of (63) that was derived in (64):

$$b_c M_1 + b_s M_2 - (b_s M_1 + b_c M_2)A + \underbrace{\big((a_s M_1 + a_c M_2)A - a_c M_1 - a_s M_2\big)}_{= a_s M_2 (A^2 - 1) > 0 \text{ in } D_3} / |x|^2.$$

Then, in $R_2 < |x| < R_1$,

$$\frac{\Lambda_2'(|x|)}{|x|} < b_c M_1 + b_s M_2 - (b_s M_1 + b_c M_2)A + a_s M_2(A^2-1)/R_2^2 \,=\, 0.$$

We conclude that (22) is violated and therefore the overlap solution is not a minimizer for $(A,B) \in D_3$.

Hence, we have shown:

Proposition 4.1 (Local minimum)**.** *The overlap solution with the lighter species inside (Figure 11) is a local minimizer in $\mathcal{F}$ with respect to class $\mathcal{B}$ perturbations for $(A,B) \in D_6$, but not for $(A,B) \in D_3$.*

As for the target equilibrium (see Theorem 3.3), we resort again to the calculations for the second variation of the energy in Section 2.2 to infer the following (much stronger) result:

Theorem 4.2 (Global minimum)**.** *The overlap equilibrium with the lighter species inside is a* global *minimizer in $\mathcal{F}_c$ for all (A,B) in D_6 with $B > 1$ ($A < 1$ holds in all D_6); i.e. in the intersection of D_6 with the shaded region in Figure 2. Note that this restriction excludes only the bounded triangular region $0 < A < B < 1$, while D_6 is unbounded.*

Therefore, by the variational approach we identified two global minimizers (overlap and target equilibria with lighter species inside) which exist in unbounded (and disjoint) subsets of the parameter space (A,B).

4.2 Heavier species inside

For this equilibrium species 1 and 2 are supported in disks of radii R_1 and R_2, respectively, with $R_1 < R_2$ – see Figure 12. The heavier species 1 is now *inside*. In $|x| < R_1$, where the two species coexist, the equilibrium densities are also given by (59) (cf. (10)). In the annular region $R_1 < |x| < R_2$, only species 2 is present, with equilibrium density (also see (10)):

$$\rho_2^{\text{out}} = \frac{b_c M_1 + b_s M_2}{\pi a_s}. \tag{65}$$

The radii of the two disks are given by

$$R_1^2 = \frac{(a_s^2 - a_c^2)M_1}{(a_s b_s - a_c b_c)M_1 + (a_s b_c - a_c b_s)M_2}, \qquad R_2^2 = \frac{a_c M_1 + a_s M_2}{b_c M_1 + b_s M_2}. \tag{66}$$

Together with the consistency condition $R_1 < R_2$, it can be shown that the overlap equilibrium above exists for $(A,B) \in D_1 \cup D_4$. Note that $A > B$ in D_1, while in D_4 one has $A < B$.

Calculate $\nabla\Lambda_1$. We find $\nabla\Lambda_1(x) = 0$ in $|x| < R_1$, as required for equilibrium (see (21)). Outside the support,

$$\frac{\Lambda_1'(|x|)}{|x|} = \begin{cases} b_s M_1 + b_c M_2 - (a_s M_1 + a_c M_2)/|x|^2 - \pi a_c \rho_2^{\text{out}}(1 - R_2^2/|x|^2) & \text{if } R_1 < |x| < R_2 \\ b_s M_1 + b_c M_2 - (a_s M_1 + a_c M_2)/|x|^2 & \text{if } |x| > R_2. \end{cases} \tag{67}$$

Consider case $(A,B) \in D_1$ first. By (66), in $|x| > R_2$ we have

$$\begin{aligned} b_s M_1 + b_c M_2 - (a_s M_1 + a_c M_2)/|x|^2 &> b_s M_1 + b_c M_2 - (a_s M_1 + a_c M_2)\frac{b_c M_1 + b_s M_2}{a_c M_1 + a_s M_2} \\ &= b_s M_2 \left(M + B - (M + A)\frac{BM+1}{AM+1} \right) \\ &= b_s M_2 \frac{(A-B)(M^2-1)}{AM+1}. \end{aligned}$$

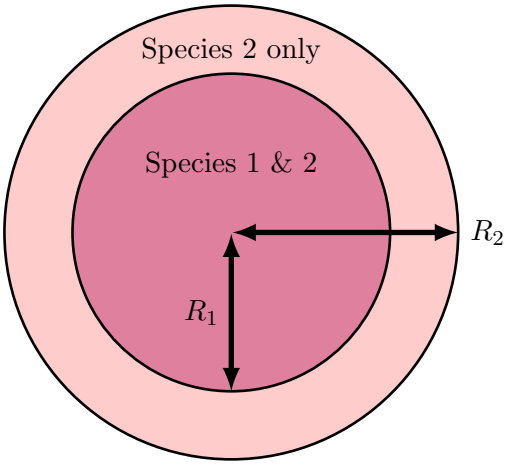

Figure 12: Overlap equilibrium, with species 1 and 2 coexisting on a disk of radius R_1, and (the lighter) species 2 also being present in the annular region $R_1 < |x| < R_2$.

As $A > B$ for $(A, B) \in D_1$ and $M > 1$, the expression above is positive, and consequently, $\Lambda_1(x)$ is radially increasing in $|x| > R_2$.

In $R_1 < |x| < R_2$, by (65) and (3), the expression on the right-hand-side of (67) can be rewritten as:

$$b_s M_1 + b_c M_2 - (b_c M_1 + b_s M_2)A + \underbrace{((a_c M_1 + a_s M_2)A - a_s M_1 - a_c M_2)}_{a_s M_2(A^2-1)M<0 \text{ in } D_1}/|x|^2 \tag{68}$$

and hence, by (66),

$$\frac{\Lambda_1'(|x|)}{|x|} > b_s M_1 + b_c M_2 - (b_c M_1 + b_s M_2)A + a_s M_2(A^2 - 1)M/R_1^2 \, = \, 0.$$

We conclude that Λ_1 is radially increasing in $|x| > R_1$ (and satisfies (22)) for all $(A, B) \in D_1$.

On the other hand, in D_4 (where $A > 1$), using (68) and an argument analogous to the above, we find that $\Lambda_1'(|x|) < 0$ and hence (22) is violated.

Finally, for Λ_2 we find $\nabla\Lambda_2(x) = 0$ in $|x| < R_2$ (as for equilibrium), and outside the support, in $|x| > R_2$:

$$\Lambda_2'(|x|) = \big((b_c M_1 + b_s M_2)|x|^2 - (a_c M_1 + a_s M_2)\big)/|x|.$$

Consequently, by the expression of R_2 in (66), Λ_2 is radially increasing in $|x| > R_2$.

In conclusion, we have shown:

Proposition 4.3. *The overlap solution with the heavier species inside is a local minimizer in $\mathcal{F}$ with respect to perturbations of class $\mathcal{B}$ when $(A, B) \in D_1$, but not for $(A, B) \in D_4$.*

Based on particle simulations we conjecture however that this overlap solution is not a minimizer with respect to class $\mathcal{A}$ perturbations for any $(A, B) \in D_1$; such an equilibrium has never been captured in simulations in fact. Unfortunately, unlike for the target solution, we do not have a linear stability analysis to support such a conjecture.

4.3 Numerical illustration: passing from D_6 to D_1

The overlap state with the lighter species inside (Section 4.1) is observed numerically as a steady state in region D_6 and we indicated this accordingly in Figure 1. Below we illustrate numerically how equilibria change when parameters cross the line $A = B$.

In Figure 13 we show a series of snapshots. The initial configuration is the overlap state that we find as the long-time steady state for $(A, B) = (0.5, 1)$. Next we change the parameters

to $(A, B) = (0.5, 0.4)$, that is, we cross the boundary between D_6 and D_1. We observe that the radial symmetry is broken, and the system attains a state in which the supports of the two species partially overlap. It turns out that, at least asymptotically close to $(A, B) = (0, 0)$, we can quantify this effect, and in particular we can find the distance between the species' centres of mass. This is done in Section 5.

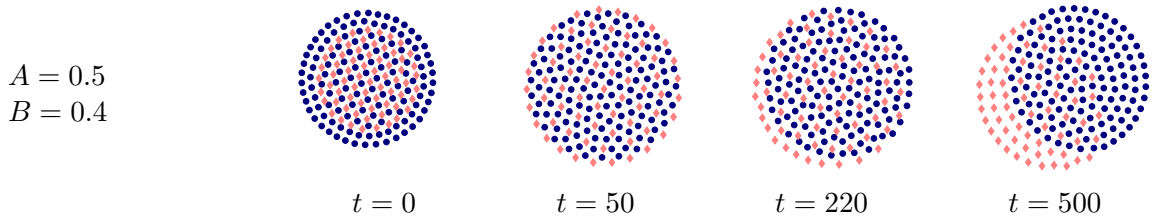

Figure 13: Steady state arising in parameter region D_1, starting from the overlap state (lighter species inside) that is stable in D_6.

5 Weak cross-interactions

Consider the case in which the cross-interactions are much weaker than the self-interactions. We consider a small parameter $0 < \eta \ll 1$ and substitute K_c by ηK_c in (1). This system exhibits a 'regular' timescale and a slow timescale (we also observe this in numerics; see Figure 14). We will now examine this separation of timescales and its implications for the steady state.

Introduce a two-scale expansion in (1) given by the variables t and $s := \eta t$. Taking the transformation $\frac{\partial}{\partial t} \mapsto \frac{\partial}{\partial t} + \eta \frac{\partial}{\partial s}$ into account, the two-scale model equations are

$$\frac{\partial \rho_1}{\partial t} + \eta \frac{\partial \rho_1}{\partial s} + \nabla \cdot (\rho_1 v_1) = 0, \quad v_1 = -\nabla K_s * \rho_1 - \eta \nabla K_c * \rho_2, \tag{69a}$$

$$\frac{\partial \rho_2}{\partial t} + \eta \frac{\partial \rho_2}{\partial s} + \nabla \cdot (\rho_2 v_2) = 0, \quad v_2 = -\eta \nabla K_c * \rho_1 - \nabla K_s * \rho_2, \tag{69b}$$

and they can be separated into

$$\mathcal{O}(\eta^0): \qquad \frac{\partial \rho_i}{\partial t} + \nabla \cdot (\rho_i(-\nabla K_s * \rho_i)) = 0, \qquad i = 1, 2, \tag{70}$$

$$\mathcal{O}(\eta^1): \qquad \frac{\partial \rho_i}{\partial s} + \nabla \cdot (\rho_i(-\nabla K_c * \rho_j)) = 0, \qquad i = 1, 2, \quad j \neq i. \tag{71}$$

Setting $\frac{\partial}{\partial t}\rho_i = 0$ and $\frac{\partial}{\partial s}\rho_i = 0$ in (70)–(71), we obtain the following conditions for a steady state:

$$-\nabla K_s * \bar{\rho}_i = 0, \quad \text{on } \operatorname{supp} \bar{\rho}_i, \text{ for each } i = 1, 2, \tag{72}$$

$$-\nabla K_c * \bar{\rho}_j = 0, \quad \text{on } \operatorname{supp} \bar{\rho}_i, \text{ for each } i = 1, 2, \quad j \neq i, \tag{73}$$

where $\bar{\rho}_1$ and $\bar{\rho}_2$ denote the steady state densities. By the first equation (72), we know that each species independently attains the steady state of a single, isolated species corresponding to the potential K_s. In fact, the zeroth-order equation (70) suggests that each species approaches this steady state at the 'regular' timescale t. Note that these steady states are determined per species up to translation of the centre of mass.

The equilibrium distance between the centres of mass can be derived from (73). Integration of $-\nabla K_c * \bar{\rho}_2 = 0$ over $\operatorname{supp} \bar{\rho}_1$ yields

$$\int_{\operatorname{supp} \bar{\rho}_1} \int_{\operatorname{supp} \bar{\rho}_2} \nabla K_c(x - y) \bar{\rho}_2(y) \bar{\rho}_1(x) \, dy dx = 0. \tag{74}$$

We note that due to the assumed antisymmetry of ∇K_c, the same condition is obtained if we integrate $-\nabla K_c * \bar{\rho}_1 = 0$ over $\operatorname{supp} \bar{\rho}_2$. This condition (74) holds for general cross-interaction potential K_c.

5.1 Newtonian-quadratic interactions

We now take the same interaction potentials K_s and K_c as in (2). By taking η small, we are zooming in at the origin in Figure 2. Analogous to (3), the dimensionless numbers A and B are defined as the ratios of the cross- and self-interaction parameters. Here we take into account that the cross-interactions are pre-multiplied by η, and we have $A := \eta\, a_c/a_s$ and $B := \eta\, b_c/b_s$.

From (72) and (2a) it follows due to [7, 26] that the steady state densities are (to leading order) of the form:

$$\bar{\rho}_1(x) = \frac{b_s\, M_1}{\pi\, a_s}\chi_{B(x_0,R)}(x), \qquad \bar{\rho}_2(x) = \frac{b_s\, M_2}{\pi\, a_s}\chi_{B(\bar{x}_0,R)}(x), \tag{75}$$

for some $x_0, \bar{x}_0 \in \mathbb{R}^2$ and with $R^2 := a_s/b_s$. Here, χ is the characteristic function. Note that both supports have the same radius, even though the masses M_1 and M_2 are in general unequal. Without loss of generality, take $\bar{x}_0 = x_0 + (d, 0)^T$ for some constant $d > 0$. The condition (74) can now be written as

$$\int_{B(x_0,R)}\int_{B(\bar{x}_0,R)} \left[a_c\, \frac{x-y}{|x-y|^2} - b_c\,(x-y)\right] dydx = 0. \tag{76}$$

and we now show that this can be reduced to a relation between d and the model parameters. The attraction part is evaluated explicitly as

$$-\, b_c \int_{B(x_0,R)}\int_{B(\bar{x}_0,R)} (x-y)\, dydx = b_c\, \pi^2 R^4(\bar{x}_0 - x_0) = \frac{a_s^2\, b_c\, \pi^2}{b_s^2}\begin{pmatrix} d \\ 0 \end{pmatrix}. \tag{77}$$

For the repulsion part, we distinguish between the following cases:

Case 1: $d > 2R$**.** In this case $B(x_0, R) \cap B(\bar{x}_0, R) = \emptyset$, hence (43) implies that for all $x \in B(x_0, R)$

$$\int_{B(\bar{x}_0,R)} \frac{x-y}{|x-y|^2}\, dy = \pi\, R^2\, \frac{x-\bar{x}_0}{|x-\bar{x}_0|^2}. \tag{78}$$

Subsequently, (43) yields that

$$\int_{B(x_0,R)} \pi\, R^2\, \frac{x-\bar{x}_0}{|x-\bar{x}_0|^2}\, dx = \pi^2\, R^4\, \frac{x_0-\bar{x}_0}{|x_0-\bar{x}_0|^2}, \tag{79}$$

because $\bar{x}_0 \notin B(x_0, R)$. Noting that $x_0 - \bar{x}_0 = (-d, 0)^T$, we conclude for $d > 2R$ that the only the first component of (76) yields a nontrivial condition. This condition is

$$-\, a_c\, \pi^2 R^4 \frac{1}{d} + b_c\, \pi^2\, R^4\, d = 0, \tag{80}$$

where we used (77) and (79). We recall that $R^2 = a_s/b_s$, $A := \eta\, a_c/a_s$ and $B := \eta\, b_c/b_s$. Hence,

$$\frac{d}{R} = \sqrt{\frac{A}{B}}. \tag{81}$$

Therefore, (81) implies that *complete separation* of the two species (that is, $d > 2R$), takes place for

$$A/B > 4.$$

Case 2: $R < d \leqslant 2R$**.** Define $B_1 := B(x_0, R) \cap B(\bar{x}_0, R)$ and $B_2 := B(x_0, R) \setminus B(\bar{x}_0, R)$. For the repulsion part of (76), it holds –cf. (43)– that

$$\begin{aligned}\int_{B(x_0,R)} \int_{B(\bar{x}_0,R)} \frac{x-y}{|x-y|^2}\, dy\, dx &= \int_{B_1} \pi\,(x-\bar{x}_0)\, dx + \int_{B_2} \pi\, R^2\, \frac{x-\bar{x}_0}{|x-\bar{x}_0|^2}\, dx \\ &= \int_{B_1} \pi\,(x-\bar{x}_0)\, dx \\ &\quad + \int_{B(x_0,R)} \pi\, R^2\, \frac{x-\bar{x}_0}{|x-\bar{x}_0|^2}\, dx - \int_{B_1} \pi\, R^2\, \frac{x-\bar{x}_0}{|x-\bar{x}_0|^2}\, dx \end{aligned} \tag{82}$$

The area of B_1 is $2R^2 \arccos(d/(2R)) - d/2\,\sqrt{4R^2 - d^2}$ while, by construction, its centre of mass is $x_0 + (d/2, 0)^T$. Therefore

$$\int_{B_1} \pi\,(x-\bar{x}_0)\, dx = \left(-\pi d \left[R^2 \arccos\left(\frac{d}{2R}\right) - \frac{d}{4}\sqrt{4R^2-d^2}\right], 0\right)^T. \tag{83}$$

For $R < d \leqslant 2R$, we have that $\bar{x}_0 \notin B(x_0, R)$. Thus, it follows from (43) that

$$\int_{B(x_0,R)} \pi\, R^2\, \frac{x-\bar{x}_0}{|x-\bar{x}_0|^2}\, dx = \pi^2\, R^4\, \frac{x_0-\bar{x}_0}{|x_0-\bar{x}_0|^2}. \tag{84}$$

It remains to evaluate the integral over B_1 in the last line of (82). For symmetry reasons, this integral is a vector in the direction of $x_0 - \bar{x}_0$, that is, in the direction of $e_1 = (1, 0)^T$. Consider therefore

$$\int_{B_1} \frac{x-\bar{x}_0}{|x-\bar{x}_0|^2}\, dx \cdot e_1 = \int_{B_1} \nabla \ln\left(\frac{|x-\bar{x}_0|}{R}\right) \cdot e_1\, dx = \int_{\partial B_1} \ln\left(\frac{|x-\bar{x}_0|}{R}\right)\; e_1 \cdot \hat{n}(x)\, dS(x), \tag{85}$$

where the last step follows from Gauss' theorem. The boundary of B_1 consists of two circular segments, that are subsets of $\partial B(x_0, R)$ and $\partial B(\bar{x}_0, R)$, respectively. Call these segments $\partial B_\alpha \subset \partial B(x_0, R)$ and $\partial B_\beta \subset \partial B(\bar{x}_0, R)$, such that $\partial B_\alpha \cup \partial B_\beta = \partial B_1$. Note that for $x \in \partial B_\beta$ it holds that $|x - \bar{x}_0| = R$, hence $\ln(|x - \bar{x}_0|/R) = 0$, and therefore the contribution of the integration over ∂B_β in (85) is zero. Thus

$$\int_{B_1} \frac{x-\bar{x}_0}{|x-\bar{x}_0|^2}\, dx \cdot e_1 = \int_{\partial B_\alpha} \ln\left(\frac{|x-\bar{x}_0|}{R}\right)\; e_1 \cdot \hat{n}(x)\, dS(x),$$

while for $x \in \partial B_\alpha$, we have $x = x_0 + R(\cos\theta, \sin\theta)^T$, $\hat{n}(x) = (\cos\theta, \sin\theta)^T$ and $dS(x) = R\, d\theta$ with $-\gamma \leqslant \theta \leqslant \gamma$ and $\gamma := \arccos(d/(2R))$. Consequently,

$$\int_{\partial B_\alpha} \ln\left(\frac{|x-\bar{x}_0|}{R}\right)\; e_1 \cdot \hat{n}(x)\, dS(x) = R \int_{-\gamma}^{\gamma} \ln\left(\sqrt{1 + \frac{d^2}{R^2} - \frac{2d}{R}\cos\theta}\right) \cos\theta\, d\theta. \tag{86}$$

A combination of (76), and (77), (82), (83), (84) and (86) yields that d/R is implicitly defined as a function of A/B by

$$\frac{A}{B} = \frac{\dfrac{d^2}{R^2}}{1 + \dfrac{d^2}{\pi R^2}\left[\gamma - \dfrac{d}{4R}\sqrt{4 - \dfrac{d^2}{R^2}}\right] + \dfrac{d}{2\pi\, R}\displaystyle\int_{-\gamma}^{\gamma} \ln\left(1 + \frac{d^2}{R^2} - \frac{2d}{R}\cos\theta\right)\cos\theta\, d\theta}. \tag{87}$$

Here we used that $R^2 = a_s/b_s$ and we recall that $\gamma = \gamma(d/R) = \arccos(d/(2R))$.

Case 3: $d \leqslant R$**.** In this case $\bar{x}_0 \in B(x_0, R)$. The only difference with the case $R < d \leqslant 2R$ is therefore the evaluation of the integral over $B(x_0, R)$ in (82). Thus, we replace (84) by

$$\int_{B(x_0,R)} \pi\, R^2\, \frac{x - \bar{x}_0}{|x - \bar{x}_0|^2}\, dx = \pi^2\, R^2\, (x_0 - \bar{x}_0) = -\pi^2\, d\, R^2\, e_1. \tag{88}$$

For $d \leqslant R$, the analogue of (87) is

$$\frac{A}{B} = \frac{\dfrac{\pi\, d}{R}}{\dfrac{\pi\, d}{R} + \dfrac{d}{R}\left[\gamma - \dfrac{d}{4R}\sqrt{4 - \dfrac{d^2}{R^2}}\right] + \dfrac{1}{2}\displaystyle\int_{-\gamma}^{\gamma} \ln\!\left(1 + \frac{d^2}{R^2} - \frac{2d}{R}\cos\theta\right)\cos\theta\, d\theta}. \tag{89}$$

We recall that $A := \eta\, a_c/a_s$ and $B := \eta\, b_c/b_s$, while $\gamma = \arccos(d/(2R))$.

Taking the limit $d \downarrow 0$ in the right-hand side of (89), we obtain $A/B = 1$. This is the threshold value for full mixing.

Consistency with densities derived in (10)**.** Note that in (75) we concluded that (to leading order) the values of the steady state densities are the same as for the single species model. That is: $\bar{\rho}_i = b_s\, M_i/(\pi\, a_s)$. In (10) we identified the steady state densities in a two-species model, and we can use these expressions to verify (75). In the setting with weak cross-interaction parameters $\eta\, a_c$ and $\eta\, b_c$, we find analogously to (10) that the equilibrium values for the density are

$$\bar{\rho}_1 = \frac{b_s M_1 + \eta\, b_c M_2}{\pi a_s} \qquad \text{in regions where only one species exists,}$$
$$\bar{\rho}_1 = \frac{(a_s b_s - \eta^2\, a_c b_c) M_1 + \eta\, (a_s b_c - a_c b_s) M_2}{\pi (a_s^2 - \eta^2 a_c^2)} \qquad \text{in overlap regions;}$$

and similar expressions for species 2. *To leading order*, these two expresions are however the same, and both are equal to the single species value $\bar{\rho}_1 = b_s\, M_1/(\pi\, a_s)$. The deviations are only $\mathcal{O}(\eta)$.

5.2 Numerical illustration

We start with an illustration of the two timescales present in the model with weak cross-interactions. We use a particle system of 100 particles with $M = 2$. That is, we have 67 particles of species 1 and 33 particles of species 2. We take $\eta = 0.001$, and furthermore $a_s = b_s = b_c = 1$ and $a_c = 6$. The particles are initialized randomly. Their time evolution is shown in Figure 14. We clearly see that each species self-organizes fast into a circular shape. The distance between the two circles equilibrates at a much larger timescale. The distance between the centres of mass of the two species is computed and divided by $R = \sqrt{a_s/b_s}$ to get an estimate for d/R (indicated above each plot in Figure 14). The values obtained slowly approach the limit value $\sqrt{A/B} = \sqrt{6} \approx 2.45$, as predicted by our asymptotic analysis; see (81).

We verify the relation between A/B and d/R provided by (81), (87) and (89). In Figure 15, the blue curve is composed of three segments corresponding to the derived expressions for $d > 2R$, $R < d \leqslant 2R$ and $d \leqslant R$, respectively. The black diamonds and stars are based on the evolution of a particle system of 200 particles. Initially they are distributed randomly. An estimate for d is obtained from the long-time configuration (at $t = 3000$), in which we compute the distance between the centres of mass of both species. We took $\eta = 0.05$, $a_s = b_s = b_c = 1$ and varied the value of a_c. Note that hence, $R = 1$.

To show that the relations between d/R and A/B are independent of the mass ratio $M = M_1/M_2$, we perform the numerical calculations for $M = 1$ (diamonds) and $M = 2$ (stars). Both

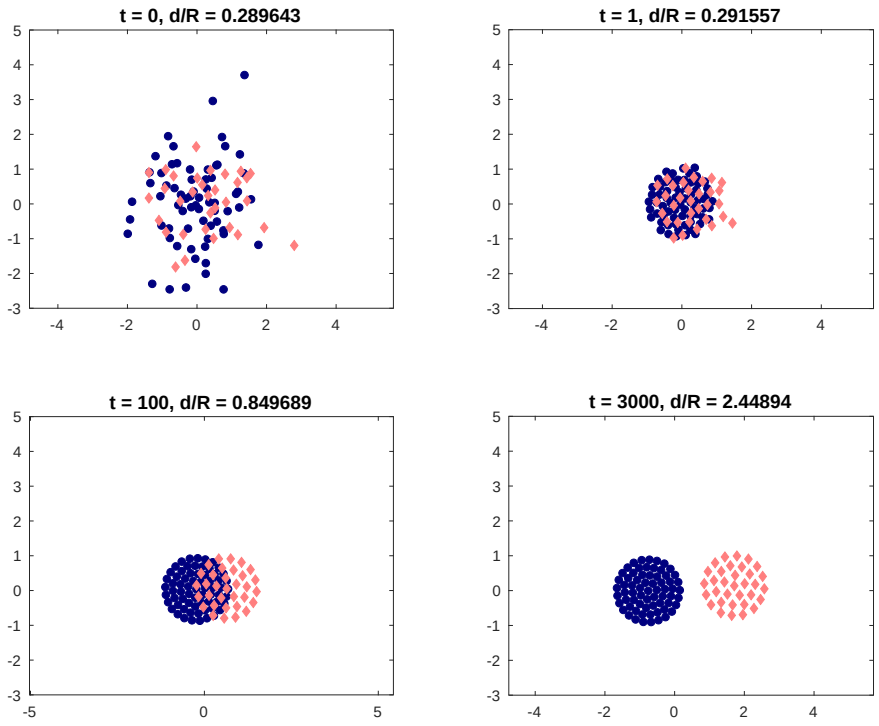

Figure 14: Time evolution of the particle system. There are 100 particles, while $M = 2$ (particles are distributed 67:33). We took $a_s = b_s = b_c = 1$ and $a_c = 6$. For each plot we indicate d/R, which is the distance between the two centres of mass divided by $R = \sqrt{a_s/b_s}$. This value approaches the theoretically derived prediction $\sqrt{A/B} = \sqrt{6} \approx 2.45$.

cases are nearly identical and coincide with the blue curve, hence confirm our prediction based on the asymptotic analysis. The blue curve also shows that $d = 0$ is attained at $A/B = 1$, the point at which a pitchfork bifurcation takes place. For $A/B < 1$, the particle system calculations exhibit full mixing, i.e. $d \approx 0$. Figure 15 contains typical examples of particle configurations for full mixing, partial overlap, tangential disks, and full separation. We will discuss these regimes now once more, using the phase plane A versus B. The weak cross-interactions regime $\eta \ll 1$ corresponds to an area infinitesimally close to the origin in the (A, B) plane. In Figure 16 we 'zoom in' near the origin and indicate which steady states we can expect to occur where. We emphasize that our considerations only hold asymptotically as $\eta \downarrow 0$.

For $A/B < 1$, we concluded that total overlap is to be expected. This happens in the area above the line $B = A$ in Figure 16. In the top configuration the two densities are supported on the same disk of radius R. Their densities may differ, depending on M. In the figure we have $M = 2$ and the density of species 1 is therefore larger than the density of species 2.

For $A/B > 1$ there is a bifurcation and steady states other than complete overlap come into existence. In Figure 15 we show the (scaled) distance between the two centres of mass being larger than zero in this case. In the phase plane (see Figure 16, below the line $B = A$) we consequently see a non-radially symmetric state in which the two species are each supported on a disk, but the centres of the disk do not coincide. See the top right configuration. There is still a region of overlap, though, as long as $A/B < 4$.

The threshold value $A/B = 4$ denotes the transition from partial overlap to full separation. For A/B we observe two tangential circular states (bottom right configuration in Figure 16). For $A/B > 4$ (that is: below the line $B = A/4$ in Figure 16) the two disks are fully separated; see the bottom left configuration. The distance between the centres of mass is predicted by the relation (81), i.e. $d/R = \sqrt{A/B}$.

In Figure 16, the lines $A/B = 1$ and $A/B = 4$ are there only for their slopes to indicate

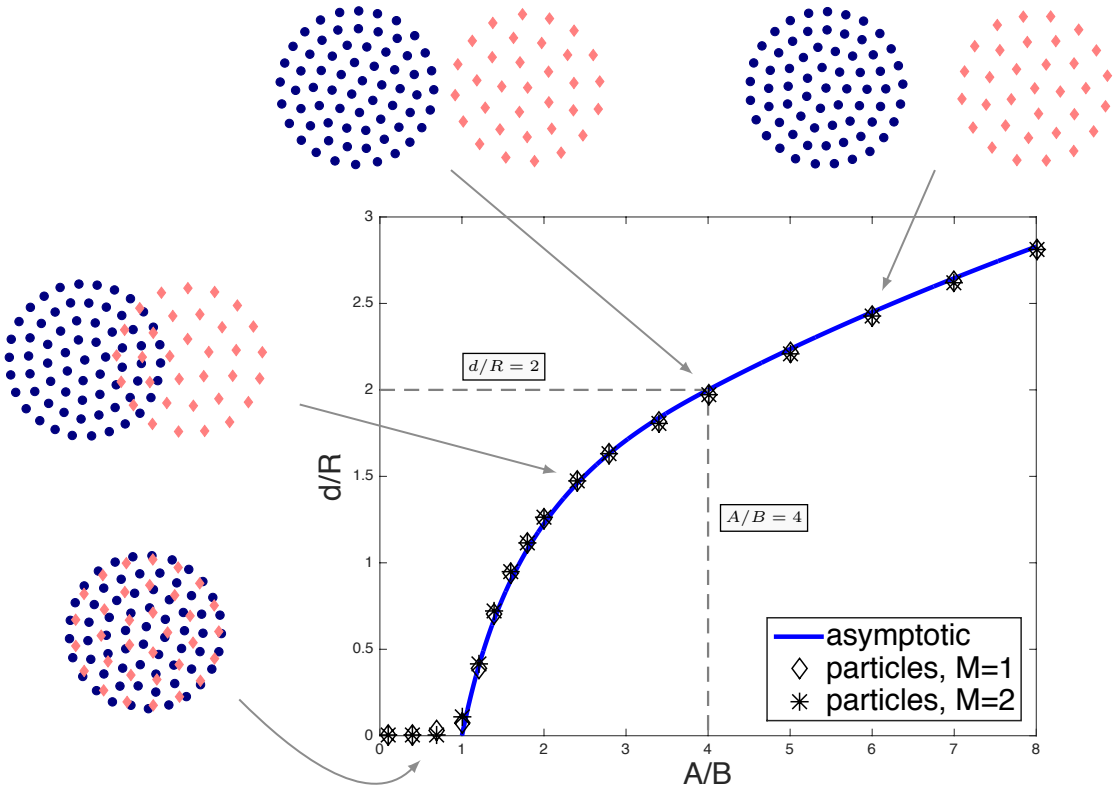

Figure 15: Blue curve: d/R as a function of A/B provided by (81), and the implicit relations (87) and (89). Data points: estimate of d/R based on particle simulations at time $t = 3000$, for $\eta = 0.05$ and several values of A/B. Black diamonds: $M = 1$, hence 100 particles per species. Black stars: similar calculations for $M = 2$, i.e. 133 particles of species 1, and 67 particles of species 2. Typical particle configurations are given to illustrate full mixing, partial overlap, tangential disks (at the point where $A/B = 4$ and $d/R = 2$), and full separation.

the *asymptotic* threshold values. If (A, B) is taken $\mathcal{O}(1)$ away from the origin, it remains to be investigated if phase plane boundaries between geometrically different steady states can be found, and whether or not these are straight lines.

6 Discussion

In this paper, we produced a catalogue of steady states for model (1) with interaction potentials (2), as presented in Figure 1.

We argued (see Section 3) by means of linear stability analysis that the target with the lighter species inside exists and is stable for parameters (A, B) in regions D_4 and D_5. The target with the heavier species inside is (if it exists at all) not stable with respect to small perturbations of the boundaries. Both results agree with what we observe numerically. Our variational approach in both cases tends to predict stability regions that are larger than those for the linear stability analysis. We expect this to be a result of the fact that in some parameter regions, due to the difficulties explained in Section 2.2, we have not considered a certain type of perturbations, namely those supported in the support of the equilibrium (referred in the paper as class $\mathcal{A}$ perturbations). Nevertheless, in the region of the parameter space where $A < 1$ and $B > 1$ we were able to do a complete variational argument to show that the the target with the

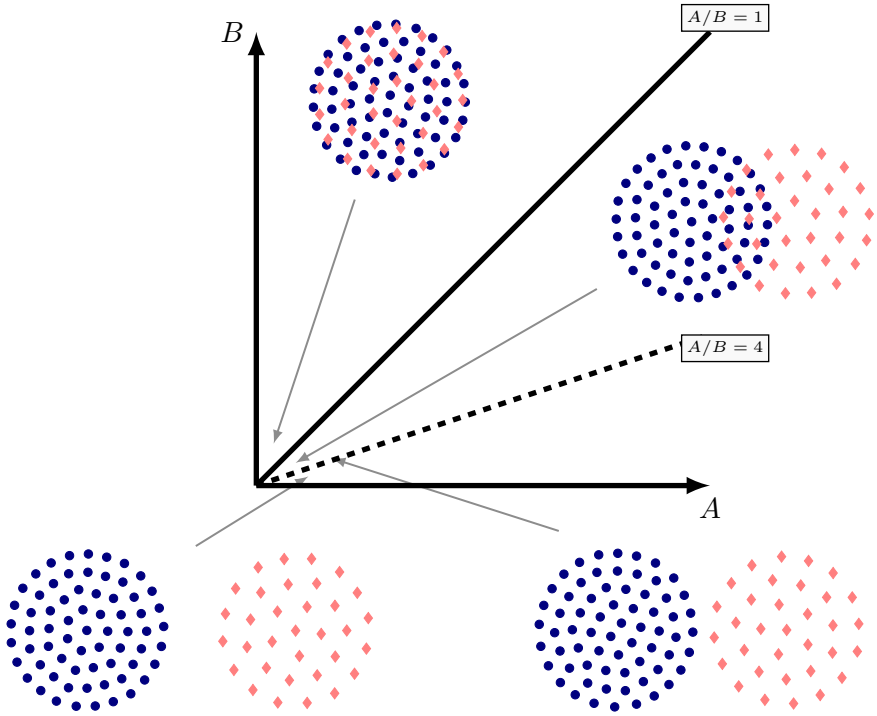

Figure 16: Steady states for weak cross-interactions depend on the value of A/B. The figure should be considered as the phase plane Figure 2 zoomed in close to the origin. The lines $A/B = 1$ and $A/B = 4$ represent the theoretically derived asymptotic thresholds for full mixing and complete separation. We observe full mixing for $A/B < 1$, partial mixing for $1 < A/B < 4$, two tangential circles for $A/B = 4$, and separation for $A/B > 4$.

lighter species inside is a global minimizer.

The 'overlap' state with the lighter species inside is numerically observed only in D_6. In Section 4 we verified this conjecture using our variational approach and found that it is a local minimizer of the energy with respect to class $\mathcal{B}$ perturbations. Moreover, in the subset of D_6 with $A < 1$ and $B > 1$ (which is all of D_6 except a bounded triangular region), a full variational analysis showed that the overlap equilibrium with the lighter species inside is a global minimizer of the energy. The overlap solution with the *heavier* species inside is never observed numerically. By the variational approach however, we found that this overlap state is a local minimizer with respect to class $\mathcal{B}$ perturbations, if and only if parameters are taken from region D_1. Based on numerical results, it is our conjecture that in D_1 this state is *not* a minimizer with respect to class $\mathcal{A}$ perturbations.

The various non-radially symmetric steady states in Figure 1 were investigated numerically in more depth. This was shown in Figures 9, 10 and 13. These states arose from initializing the system (39) in a radially symmetric configuration and taking parameters outside the corresponding stability region. We were able to observe the specific modes of instability.

Finally we shed light on the symmetry-breaking that happens when passing parameters from D_6 to D_1. In Section 5 we examined the limit of weak cross interactions and obtained an (asymptotically valid) relation between the parameters (A, B) and the distance between the centres of mass of the two species.

The choice of potentials (2) in this paper is quite specific. Our main motivation for taking these Newtonian-quadratic potentials is the fact that they leave room for obtaining results analytically. For instance, the fact that all steady states in this paper are "piecewise" constant, is a direct result of the choice of potentials. Our method of performing linear stability analysis was

inspired by this observation. However, from the point of view of the biological applications, one might prefer alternative potentials that induce interactions with a limited range. We acknowledge that potentials (2) even lead to *increasing* attraction as the distance grows. One should be aware however that different potentials will lead inevitably to changes in the nature of the steady states.

A less radical way to increase realism is to remove the symmetry in the interactions between species 1 and 2. There is no direct biological reason why the two respective species among themselves would behave according to the same parameters. Neither is there a reason why species 1 would respond in the same way to species 2 as species 2 responds to species 1. Instead of having two repulsion parameters a_s and a_c, one could therefore introduce four parameters: a_{11}, a_{22} for self-repulsion and a_{12}, a_{21} for cross-repulsion. The analogue can be done for the attraction parameters b_s and b_c. We note that such modifications may alter the dynamics of the system (e.g. introducing chasing dynamics). Moreover, the resulting system will in general no longer possess the gradient flow structure. Consequently, the variational approach of this paper may be not applicable anymore, and other methods for investigation of stability need to be designed.

Furthermore, making the step from a one-species model to a two-species model naturally opens the door to exploring multi-species models. Some preliminary numerical experiments for three species (not presented in the current paper) indicate that many interesting patterns may be expected.

A Target equilibrium with $(A, B) \in D_3$: condition (22) for Λ_2

With parameters $(A, B) \in D_3$, checking condition (22) for Λ_2 amounts to comparing the relative sizes of λ_2 and λ_m – see Figures 5(b) and (c). To find λ_2 and λ_m, we use (42) and calculate $\Lambda_2(x)$ in $|x| < R_2$ (where Λ_2 has constant value λ_2) and at the location (47). We find

$$\begin{aligned}\lambda_2 = &\frac{1}{2}(a_c M_1 + a_s M_2) - \bar{\rho}_1 a_c(\pi R_0^2 \log R_0 - \pi R_1^2 \log R_1) - \bar{\rho}_2 a_s \pi R_2^2 \log R_2 \\ &+ \frac{1}{4}(b_c M_1(R_0^2 + R_1^2) + b_s M_2 R_2^2),\end{aligned} \tag{90}$$

and

$$\begin{aligned}\lambda_m = &\frac{1}{2}(a_c M_1 + a_s M_2) - \frac{1}{2}(a_c M_1 + a_s M_2)\log\left(\frac{a_c M_1 + a_s M_2}{b_c M_1 + b_s M_2}\right) \\ &+ \frac{1}{4}(b_c M_1(R_0^2 + R_1^2) + b_s M_2 R_2^2).\end{aligned} \tag{91}$$

Note that the first term in the right-hand-sides of (90) and (91), as well as the expressions on the second lines of the respective right-hand-sides, are the same. Also, by adding and subtracting $\bar{\rho}_1 a_c \pi R_1^2 \log R_0$ one can write

$$\bar{\rho}_1 a_c(\pi R_0^2 \log R_0 - \pi R_1^2 \log R_1) + \bar{\rho}_2 a_s \pi R_2^2 \log R_2 = a_c M_1 \log R_0 + a_s M_2 \log R_2 + \bar{\rho}_1 a_c \pi R_1^2 \log\left(\frac{R_0}{R_1}\right).$$

Use the above in the expression (90) for λ_2. The target is not a minimizer if $\lambda_m < \lambda_2$. By (90) and (91), this occurs when

$$\frac{1}{2}(a_c M_1 + a_s M_2)\log\left(\frac{a_c M_1 + a_s M_2}{b_c M_1 + b_s M_2}\right) > a_c M_1 \log R_0 + a_s M_2 \log R_2 + \bar{\rho}_1 a_c \pi R_1^2 \log\left(\frac{R_0}{R_1}\right).$$

By using (40) and notations (3), we can reduce the inequality above to

$$AM \log\left(\frac{BM+1}{B+M}\right) - AM \log\left(\frac{AM+1}{A+M}\right) - \log(1+AM) < -A^2 \log\left(1 + \frac{M}{A}\right),$$

and after some elementary manipulations, one finds (48).

B Calculation of the basic integrals for perturbed boundaries

For brevity of notation, in this appendix we omit any t-dependence in the perturbations. We evaluate integrals (37) on the perturbed boundaries; that is, for $x = p_j(\theta_0)$ for some index j. The latter integral in (37) becomes

$$\int_{\Omega_\ell^\varepsilon} (x-y)\,dy = x\int_{\Omega_\ell^\varepsilon} dy \;-\int_{\Omega_\ell^\varepsilon} y\,dy = \begin{cases} x\,\pi R_\ell^2 - \pi R_\ell^3\,\varepsilon_{\ell,N} & \text{if } m=1,\\ x\,\pi R_\ell^2 & \text{if } m\geqslant 2; \end{cases} \tag{92}$$

where second- and higher-order terms in $\underline{\varepsilon}$ are omitted. Here we used the full expressions for the area and centre of mass of Ω_ℓ^ε as given in Section 2.3. Note that by taking $x = p_j(\theta_0)$, we introduce extra $\mathcal{O}(\underline{\varepsilon})$ terms in (92).

To find the first-order approximation of the first integral in (37), we take $x = p_j(\theta_0)$, parameterize $\partial\Omega_\ell^\varepsilon$ by $p_\ell(\theta)$ and compute that

$$\hat{n}\,dS = R_\ell\,e^{i\theta}(1 + (\varepsilon_{\ell,N} + m\varepsilon_{\ell,T})\cos(m\theta) + i\,(\varepsilon_{\ell,T} + m\varepsilon_{\ell,N})\sin(m\theta))\,d\theta. \tag{93}$$

Subsequently, we obtain

$$\begin{aligned} &-\int_{\partial\Omega_\ell^\varepsilon} \ln|x-y|\,\hat{n}\,dS = \\ &-\int_0^{2\pi} \ln(|p_j(\theta_0) - p_\ell(\theta)|)\,R_\ell\,e^{i\theta}(1 + (\varepsilon_{\ell,N} + m\varepsilon_{\ell,T})\cos(m\theta) + i\,(\varepsilon_{\ell,T} + m\varepsilon_{\ell,N})\sin(m\theta))\,d\theta. \end{aligned} \tag{94}$$

The logarithm in the integrand can be written as

$$\ln|p_j(\theta_0) - p_\ell(\theta)| = \frac{1}{2}\ln|p_j(\theta_0) - p_\ell(\theta)|^2$$

and we expand it in terms of $\underline{\varepsilon}$. First, we expand:

$$\begin{aligned} |p_j(\theta_0) - p_\ell(\theta)|^2 = {} & \overbrace{|R_j\,e^{i\theta_0} - R_\ell\,e^{i\theta}|^2}^{=R_j^2+R_\ell^2-2R_jR_\ell\cos(\theta-\theta_0)} \\ & + \varepsilon_{j,N} 2R_j\,\cos(m\theta_0)\cdot(R_j - R_\ell\cos(\theta-\theta_0)) \\ & + \varepsilon_{\ell,N} 2R_\ell\,\cos(m\theta)\cdot(R_\ell - R_j\cos(\theta-\theta_0)) \\ & - 2R_jR_\ell\sin(\theta-\theta_0)\cdot(\varepsilon_{j,T}\sin(m\theta_0) - \varepsilon_{\ell,T}\sin(m\theta)) + \mathcal{O}(|\underline{\varepsilon}|^2). \end{aligned} \tag{95}$$

Here, we use the generic notation $\mathcal{O}(|\underline{\varepsilon}|^2)$ for higher-order terms in any $\varepsilon_{j,N}$, $\varepsilon_{j,T}$, $\varepsilon_{\ell,N}$ or $\varepsilon_{\ell,T}$. Introduce the notation $\alpha := R_\ell/R_j$. We use (95) and $\ln(X+\varepsilon Y) \sim \ln(X) + \varepsilon Y/X$ in (94), we omit further $\mathcal{O}(|\underline{\varepsilon}|^2)$ terms and write sines and cosines as complex exponentials. After expanding (94) in this way, there is a part containing a logarithm that consists of integrals of the form

$$\int_0^{2\pi} \ln(1+\alpha^2 - 2\alpha\cos(\theta-\theta_0))\,e^{i\mu\theta}\,d\theta = -\frac{2\pi}{|\mu|}\,e^{i\mu\theta_0}\begin{cases}\alpha^{|\mu|} & \text{if } \alpha\leqslant 1,\\ \alpha^{-|\mu|} & \text{if } \alpha>1;\end{cases} \tag{96}$$

for several values of $\mu \in \mathbb{Z}\setminus\{0\}$. The expression in (96) is derived in Appendix C and is valid for any $\alpha > 0$, including $\alpha = 1$. Note that $\ln(R_j^2 + R_\ell^2 - 2R_jR_\ell\cos(\theta-\theta_0)) = \ln(R_j^2) + \ln(1+\alpha^2 - 2\alpha\cos(\theta-\theta_0))$, while one can show that the part of (94) containing $\ln(R_j^2)$ has zero contribution eventually. Consequently, the "logarithmic part" of (94), equals

$$\begin{cases} \pi R_\ell e^{i\theta_0}\left(\beta + \dfrac{1}{2}(\varepsilon_{\ell,N}+\varepsilon_{\ell,T})\beta^2 e^{i\theta_0}\right) & \text{if } m=1,\\[2ex] \pi R_\ell e^{i\theta_0}\left(\beta + \dfrac{1}{2}(\varepsilon_{\ell,N}+\varepsilon_{\ell,T})\beta^{m+1}e^{im\theta_0} - \dfrac{1}{2}(\varepsilon_{\ell,N}-\varepsilon_{\ell,T})\beta^{m-1}e^{-im\theta_0}\right) & \text{if } m\neq 1; \end{cases} \tag{97}$$

with $\beta := \min\{R_j, R_\ell\}/\max\{R_j, R_\ell\} \leqslant 1$.

There is a "rational part" in (94) that, for $\alpha \neq 1$, consists of contributions of the form

$$\int_0^{2\pi} \frac{e^{i\mu\theta}}{1+\alpha^2-2\alpha\cos(\theta-\theta_0)}\,d\theta = 2\pi e^{i\mu\theta_0}\begin{cases}\dfrac{\alpha^{|\mu|}}{1-\alpha^2} & \text{if } \alpha<1,\\[2ex] \dfrac{\alpha^{-|\mu|}}{\alpha^2-1} & \text{if } \alpha>1.\end{cases} \tag{98}$$

This expression is also derived in Appendix C and it is valid for all $\mu \in \mathbb{Z}$.

The "rational part" of (94) becomes (for $\alpha \neq 1$):

$$\begin{cases} -\dfrac{R_\ell}{2}\pi\alpha e^{i\theta_0}\Big[\Big(\varepsilon_{j,N}-\varepsilon_{j,T}-\alpha(\varepsilon_{\ell,N}-\varepsilon_{\ell,T})\Big)e^{i\theta_0}+(\varepsilon_{j,N}+\varepsilon_{j,T})\,e^{-i\theta_0}\Big] & \text{if } m=1 \text{ and } \alpha<1,\\[2ex] -\dfrac{R_\ell}{2}\pi\alpha e^{i\theta_0}\Big[\Big(\varepsilon_{j,N}-\varepsilon_{j,T}-\alpha^m(\varepsilon_{\ell,N}-\varepsilon_{\ell,T})\Big)e^{im\theta_0} & \\ \qquad +\Big(\varepsilon_{j,N}+\varepsilon_{j,T}-\alpha^{m-2}(\varepsilon_{\ell,N}-\varepsilon_{\ell,T})\Big)e^{-im\theta_0}\Big] & \text{if } m\neq 1 \text{ and } \alpha<1,\\[2ex] \dfrac{R_\ell}{2}\dfrac{\pi}{\alpha}e^{i\theta_0}\Big[\Big(\varepsilon_{j,N}+\varepsilon_{j,T}-\dfrac{1}{\alpha}(\varepsilon_{\ell,N}+\varepsilon_{\ell,T})\Big)e^{i\theta_0}+\Big(\varepsilon_{j,N}-\varepsilon_{j,T}-2\alpha\varepsilon_{\ell,N}\Big)e^{-i\theta_0}\Big] & \text{if } m=1 \text{ and } \alpha>1,\\[2ex] \dfrac{R_\ell}{2}\dfrac{\pi}{\alpha}e^{i\theta_0}\Big[\Big(\varepsilon_{j,N}+\varepsilon_{j,T}-\alpha^{-m}(\varepsilon_{\ell,N}+\varepsilon_{\ell,T})\Big)e^{im\theta_0} & \\ \qquad +\Big(\varepsilon_{j,N}-\varepsilon_{j,T}-\alpha^{2-m}(\varepsilon_{\ell,N}+\varepsilon_{\ell,T})\Big)e^{-im\theta_0}\Big] & \text{if } m\neq 1 \text{ and } \alpha>1. \end{cases} \tag{99}$$

This approach is correct as long as $j \neq \ell$, since otherwise $R_j = R_\ell$, thus $\alpha = 1$, and there is a singularity in the denominator. This case requires a partially different approach. If $j = \ell$, then the rational $\mathcal{O}(\underline{\varepsilon})$ part becomes

$$\begin{aligned} -\frac{R_j}{2}\int_0^{2\pi}\Big[\varepsilon_{j,N}\cos(m\theta_0)+\varepsilon_{j,N}\cos(m\theta)+\varepsilon_{j,T}\Big(\sin(m\theta)-\sin(m\theta_0)\Big)\frac{\sin(\theta-\theta_0)}{1-\cos(\theta-\theta_0)}\Big]\,e^{i\theta}\,d\theta \\ = \begin{cases} -\dfrac{R_j}{2}\pi(\varepsilon_{j,N}+\varepsilon_{j,T}) & \text{if } m=1,\\[2ex] -R_j\pi\,\varepsilon_{j,T}\,e^{-i(m-1)\theta_0} & \text{if } m\neq 1. \end{cases} \end{aligned} \tag{100}$$

In the latter part of the integrand the singularity in the denominator is compensated by the terms in the numerator, which can be seen by expanding all sines and cosines in complex exponentials. Note that if we take $j = \ell$, we see that the limits $\alpha \downarrow 1$ and $\alpha \uparrow 1$ in (99) agree and are equal to the expressions in (100) for both $m = 1$ and $m \neq 1$.

In conclusion, combining (97), (99) and (100), we have the following:

Case $R_\ell < R_j$, hence $\alpha < 1$ and $\beta = \alpha = R_\ell/R_j$: For all $m \geqslant 1$,

$$\begin{aligned} \int_{\Omega_\ell^\varepsilon}\frac{x-y}{|x-y|^2}\,dy &= \pi R_\ell e^{i\theta_0}\left[\beta-\left(\frac{1}{2}\beta(\varepsilon_{j,N}-\varepsilon_{j,T})-\beta^{m+1}\,\varepsilon_{\ell,N}\right)e^{im\theta_0}-\frac{1}{2}\beta(\varepsilon_{j,N}+\varepsilon_{j,T})e^{-im\theta_0}\right] \\ &= \pi R_\ell e^{i\theta_0}\left[\beta+\left(-\beta\varepsilon_{j,N}+\beta^{m+1}\varepsilon_{\ell,N}\right)\cos(m\theta_0)+\left(\beta\varepsilon_{j,T}+\beta^{m+1}\varepsilon_{\ell,N}\right)\,i\sin(m\theta_0)\right]. \end{aligned} \tag{101}$$

Case $\ell = j$, hence $R_\ell = R_j$ and $\beta = \alpha = 1$: For all $m \geqslant 1$,

$$\begin{aligned} \int_{\Omega_\ell^\varepsilon}\frac{x-y}{|x-y|^2}\,dy &= \pi R_j e^{i\theta_0}\left[1+\frac{1}{2}(\varepsilon_{j,N}+\varepsilon_{j,T})e^{im\theta_0}-\frac{1}{2}(\varepsilon_{j,N}+\varepsilon_{j,T})e^{-im\theta_0}\right] \\ &= \pi R_j e^{i\theta_0}\left[1+(\varepsilon_{j,N}+\varepsilon_{j,T})\,i\sin(m\theta_0)\right]. \end{aligned} \tag{102}$$

Case $R_\ell > R_j$, hence $\alpha > 1$ and $\beta = 1/\alpha = R_j/R_\ell$: For all $m \geqslant 1$,

$$\int_{\Omega_\ell^\varepsilon} \frac{x-y}{|x-y|^2}\,dy = \pi R_\ell e^{i\theta_0}\left[\beta + \frac{1}{2}\beta(\varepsilon_{j,N}+\varepsilon_{j,T})e^{im\theta_0} + \left(\frac{1}{2}\beta(\varepsilon_{j,N}-\varepsilon_{j,T}) - \beta^{m-1}\varepsilon_{\ell,N}\right)e^{-im\theta_0}\right]$$
$$= \pi R_\ell e^{i\theta_0}\left[\beta + \left(\beta\varepsilon_{j,N} - \beta^{m-1}\varepsilon_{\ell,N}\right)\cos(m\theta_0) + \left(\beta\varepsilon_{j,T} + \beta^{m-1}\varepsilon_{\ell,N}\right) i\sin(m\theta_0)\right]. \quad (103)$$

Note that the above expressions are consistent in the sense that if we set $j = \ell$ (hence, $\beta = 1$) in either (101) or (103) we obtain (102). Note also that if we set $\varepsilon_{j,N} = \varepsilon_{j,T} = \varepsilon_{\ell,N} = \varepsilon_{\ell,T} = 0$ in (101)-(102)-(103), the expressions are consistent with (43).

C Evaluation of integrals (96) and (98)

The integral on the left-hand side of (98) is treated as follows:

$$\int_0^{2\pi} \frac{e^{i\mu\theta}}{1+\alpha^2-2\alpha\cos(\theta-\theta_0)}\,d\theta = e^{i\mu\theta_0}\int_{-\pi}^{\pi}\frac{e^{i\mu\phi}}{1+\alpha^2-2\alpha\cos(\phi)}\,d\phi,$$

where the substitution $\phi = \theta - \theta_0$ is used. The real part of the integrand on the right-hand side is an even function in ϕ, while the imaginary part is odd. Hence,

$$\int_{-\pi}^{\pi}\frac{e^{i\mu\phi}}{1+\alpha^2-2\alpha\cos(\phi)}\,d\phi = 2\int_0^{\pi}\frac{\cos(\mu\phi)}{1+\alpha^2-2\alpha\cos(\phi)}\,d\phi.$$

The latter integral is given in [32, p. 253, No. 31]. Note that [32] only treats $\mu \geqslant 0$, but that the expression given therein is easily generalized to all $\mu \in \mathbb{Z}$. The above considerations combined yield (98).

To find (96), we compute the derivative of the left-hand side with respect to θ_0 in two different ways. On the one hand:

$$\frac{d}{d\theta_0}\int_0^{2\pi}\ln(1+\alpha^2-2\alpha\cos(\theta-\theta_0))\,e^{i\mu\theta}\,d\theta = \int_0^{2\pi}\frac{-2\alpha\sin(\theta-\theta_0)}{1+\alpha^2-2\alpha\cos(\theta-\theta_0)}\,e^{i\mu\theta}\,d\theta$$
$$= -2\alpha\,e^{i\mu\theta_0}\int_0^{2\pi}\frac{\sin(\phi)}{1+\alpha^2-2\alpha\cos(\phi)}\,e^{i\mu\phi}\,d\phi. \quad (104)$$

Again, we used the substitution $\phi = \theta - \theta_0$. Writing $\sin\phi$ in terms of complex exponentials $\sin\phi = (\exp(i\phi) - \exp(-i\phi))/(2i)$, we can express the latter integral as the difference of two integrals of the form (98). By working out the result for all $\mu \in \mathbb{Z}\setminus\{0\}$, we obtain

$$-2\alpha\,e^{i\mu\theta_0}\int_0^{2\pi}\frac{\sin(\phi)}{1+\alpha^2-2\alpha\cos(\phi)}\,e^{i\mu\phi}\,d\phi = \begin{cases} -2\pi i\,e^{i\mu\theta_0}\operatorname{sgn}(\mu)\,\alpha^{|\mu|} & \text{if } \alpha < 1,\\ -2\pi i\,e^{i\mu\theta_0}\operatorname{sgn}(\mu)\,\alpha^{-|\mu|} & \text{if } \alpha > 1.\end{cases} \quad (105)$$

On the other hand:

$$\frac{d}{d\theta_0}\int_0^{2\pi}\ln(1+\alpha^2-2\alpha\cos(\theta-\theta_0))\,e^{i\mu\theta}\,d\theta = i\,\mu\,e^{i\mu\theta_0}\int_0^{2\pi}\ln(1+\alpha^2-2\alpha\cos(\phi))\,e^{i\mu\phi}\,d\phi$$
$$= i\,\mu\int_0^{2\pi}\ln(1+\alpha^2-2\alpha\cos(\theta-\theta_0))\,e^{i\mu\theta}\,d\theta \quad (106)$$

Together, (104), (105) and (106) yield the result of (96) in all cases except for $\alpha = 1$.

For $\alpha = 1$ (and $\mu \neq 0$), note that the imaginary part of the integrand $\ln(2-2\cos(\phi))\,\exp(i\mu\phi)$ is an odd function, and therefore yields no contribution. Therefore,

$$\int_0^{2\pi}\ln(2-2\cos(\theta-\theta_0))\,e^{i\mu\theta}\,d\theta = e^{i\mu\theta_0}\int_0^{2\pi}\ln(2-2\cos(\phi))\,\cos(\mu\phi)\,d\phi$$

and integration by parts yields

$$\int_0^{2\pi} \ln(2-2\cos(\phi))\,\cos(\mu\phi)\,d\phi = \left[\frac{1}{\mu}\sin(\mu\phi)\ln\Big(2-2\cos(\phi)\Big)\right]_0^{2\pi} - \frac{1}{\mu}\int_0^{2\pi}\frac{\sin(\mu\phi)\,\sin(\phi)}{1-\cos(\phi)}d\phi. \tag{107}$$

The boundary terms vanish, and this can be shown by introducing series expansions around 0 and 2π and applying l'Hôpital's rule. Moreover, the integrand on the right-hand side has no singularities. To see this, expand all sines and cosines in complex exponentials (analogously to the arguments leading to (100)). Some manipulations are required to observe that all apparent singularities are compensated by zeros in the numerator. Having done these manipulations, we can evaluate the integral exactly, multiplying by $\exp(i\mu\theta_0)$, we obtain the right-hand side of (96), for $\alpha = 1$.

Acknowledgements

This research was funded in part by Canada's National Science and Engineering Research Council (NSERC) through grants to RF and TK.

References

[1] N.J. Armstrong, K.J. Painter, and J.A. Sherratt. A continuum approach to modelling cell-cell adhesion. *Journal of Theoretical Biology*, 243:98–113, 2006.

[2] D. Balagué, J. A. Carrillo, T. Laurent, and G. Raoul. Dimensionality of local minimizers of the interaction energy. *Arch. Ration. Mech. Anal.*, 209(3):1055–1088, 2013.

[3] D. Balagué, J. A. Carrillo, T. Laurent, and G. Raoul. Nonlocal interactions by repulsive-attractive potentials: radial ins/stability. *Phys. D*, 260:5–25, 2013.

[4] J. Berendsen, M. Burger, and J.-F. Pietschmann. On a cross-diffusion model for multiple species with nonlocal interaction and size exclusion. `arXiv:1609.05024`, 2016.

[5] Andrew J. Bernoff and Chad M. Topaz. A primer of swarm equilibria. *SIAM J. Appl. Dyn. Syst.*, 10(1):212–250, 2011.

[6] Andrea L. Bertozzi, José A. Carrillo, and Thomas Laurent. Blow-up in multidimensional aggregation equations with mildly singular interaction kernels. *Nonlinearity*, 22(3):683–710, 2009.

[7] Andrea L. Bertozzi, Thomas Laurent, and Leger Flavien. Aggregation and Spreading via the Newtonian Potential: The Dynamics of Patch Solutions. *Math. Models Methods Appl. Sci.*, 22(Supp. 1):1140005, 2012.

[8] Andrea L. Bertozzi, Thomas Laurent, and Jesus Rosado. L^p theory for the multidimensional aggregation equation. *Comm. Pur. Appl. Math.*, 64(1):45–83, 2011.

[9] M. Bodnar and J. J. L. Velazquez. An integro-differential equation arising as a limit of individual cell-based models. *J. Differential Equations*, 222(2):341–380, 2006.

[10] Paul C Bressloff. Waves in neural media. *Lecture Notes on Mathematical Modelling in the Life Sciences (Springer, New York, 2014)*, 2014.

[11] G.W. Brodland. The Differential Interfacial Tension Hypothesis (DITH): A comprehensive theory for the self-rearrangement of embryonic cells and tissues. *ASME Journal of Biomechanical Engineering*, 124:188–197, 2002.

[12] J. A. Cañizo, J. A. Carrillo, and F. S. Patacchini. Existence of compactly supported global minimisers for the interaction energy. *Arch. Ration. Mech. Anal.*, 217(3):1197–1217, 2015.

[13] J. A. Carrillo, M. DiFrancesco, A. Figalli, T. Laurent, and D. Slepčev. Global-in-time weak measure solutions and finite-time aggregation for nonlocal interaction equations. *Duke Math. J.*, 156(2):229–271, 2011.

[14] José Antonio Carrillo, Young-Pil Choi, and Maxime Hauray. The derivation of swarming models: mean-field limit and Wasserstein distances. In *Collective dynamics from bacteria to crowds*, volume 553 of *CISM Courses and Lectures*, pages 1–46. Springer, Vienna, 2014.

[15] Yuxin Chen and Theodore Kolokolnikov. A minimal model of predator-swarm dynamics. *J. R. Soc. Interface*, 11(94):20131208, 2014.

[16] Rustum Choksi, Razvan C. Fetecau, and Ihsan Topaloglu. On minimizers of interaction functionals with competing attractive and repulsive potentials. *Ann. Inst. H. Poincaré Anal. Non Linéaire*, 32(6):1283–1305, 2015.

[17] M. Cicalese, L. De Luca, M. Novaga, and M. Ponsiglione. Ground States of a Two Phase Model with Cross and Self Attractive Interactions. *SIAM J. Math. Anal.*, 48(5):3412–3443, 2016.

[18] Stephen Coombes, Helmut Schmidt, and Ingo Bojak. Interface dynamics in planar neural field models. *J. Math. Neurosci.*, 2:Art. 9, 27, 2012.

[19] Gianluca Crippa and Magali Lécureux-Mercier. Existence and uniqueness of measure solutions for a system of continuity equations with non-local flow. *NoDEA Nonlinear Differential Equations Appl.*, 20(3):523–537, 2013.

[20] M. Desroches D. Avitabile and E. Knobloch. Spatiotemporal canards in neural field equations. *Phys. Rev. E*, 95:042205, 2017.

[21] Marco Di Francesco and Simone Fagioli. Measure solutions for non-local interaction PDEs with two species. *Nonlinearity*, 26(10):2777–2808, 2013.

[22] Marco Di Francesco and Simone Fagioli. A nonlocal swarm model for predators-prey interactions. *Math. Models Methods Appl. Sci.*, 26(2):319–355, 2016.

[23] Joep H. M. Evers, Sander C. Hille, and Adrian Muntean. Measure-valued mass evolution problems with flux boundary conditions and solution-dependent velocities. *SIAM J. Math. Anal.*, 48(3):1929–1953, 2016.

[24] Klemens Fellner and Gael Raoul. Stable stationary states of non-local interaction equations. *Math. Models Methods Appl. Sci.*, 20(12):2267–2291, 2010.

[25] Razvan C. Fetecau and Yanghong Huang. Equilibria of biological aggregations with nonlocal repulsive-attractive interactions. *Physica D*, 260:49–64, 2013.

[26] Razvan C. Fetecau, Yanghong Huang, and Theodore Kolokolnikov. Swarm dynamics and equilibria for a nonlocal aggregation model. *Nonlinearity*, 24(10):2681–2716, 2011.

[27] Stefanos E. Folias and Paul C. Bressloff. Breathers in two-dimensional neural media. *Phys. Rev. Lett.*, 95(20):208107, 2005.

[28] Stefanos E. Folias and G. Bard Ermentrout. Bifurcations of stationary solutions in an interacting pair of E-I neural fields. *SIAM J. Appl. Dyn. Syst.*, 11(3):895–938, 2012.

[29] R.A. Foty, C.M. Pfleger, G. Forgacs, and M.S. Steinberg. Surface tensions of embryonic tissues predict their mutual envelopment behavior. *Development*, 122:1611–1620, 1996.

[30] Yanghong Huang and Andrea L. Bertozzi. Self-similar blowup solutions to an aggregation equation in $\mathbb{R}^n$. *SIAM J. Appl. Math.*, 70(7):2582–2603, 2010.

[31] Barry D. Hughes and Klemens Fellner. Continuum models of cohesive stochastic swarms: the effect of motility on aggregation patterns. *Physica D*, 260:26–48, 2013.

[32] A. Jeffrey. *Handbook of Mathematical Formulas and Integrals.* Academic Press, second edition, 2000.

[33] T. Kolokolnikov, P.G. Kevrekidis, and R. Carretero-González. A tale of two distributions: from few to many vortices in quasi-two-dimensional Bose-Einstein condensates. *Proc. R. Soc. A*, 470:20140048, 2014.

[34] Theodore Kolokolnikov, Hui Sun, David Uminsky, and Andrea L. Bertozzi. A theory of complex patterns arising from 2D particle interactions. *Phys. Rev. E, Rapid Communications*, 84:015203(R), 2011.

[35] N. S. Landkof. *Foundations of Modern Potential Theory.* Springer-Verlag, New York-Heidelberg, 1972. Translated from the Russian by A. P. Doohovskoy, Die Grundlehren der mathematischen Wissenschaften, Band 180.

[36] Andrew J. Leverentz, Chad M. Topaz, and Andrew J. Bernoff. Asymptotic dynamics of attractive-repulsive swarms. *SIAM J. Appl. Dyn. Syst.*, 8(3):880–908, 2009.

[37] Alan Mackey, Theodore Kolokolnikov, and Andrea L. Bertozzi. Two-species particle aggregation and stability of co-dimension one solutions. *Discrete Contin. Dyn. Syst. Ser. B*, 19(5):1411–1436, 2014.

[38] K.J. Painter, J.M. Bloomfield, J.A. Sherratt, and A. Gerisch. A nonlocal model for contact attraction and repulsion in heterogeneous cell populations. *Bull Math Biol*, 77:1132–1165, 2015.

[39] R. Simione, D. Slepčev, and I. Topaloglu. Existence of ground states of nonlocal-interaction energies. *J. Stat. Phys.*, 159(4):972–986, 2015.

[40] James von Brecht, David Uminsky, Theodore Kolokolnikov, and Andrea Bertozzi. Predicting pattern formation in particle interactions. *Math. Models Methods Appl. Sci.*, 22(Supp. 1):1140002, 2012.